이학박사 학위논문

SI-STM Study on Novel Fe Based Superconductor $Ca_{0.9}La_{0.1}FeAs_2$

새로운 초전도체 $Ca_{0.9}La_{0.1}FeAs_2$에 대한 SI-STM 연구

2020년 8월

서울대학교 대학원

물리천문학부

김 재 준

SI-STM Study on Novel Fe Based Superconductor $Ca_{0.9}La_{0.1}FeAs_2$

지도 교수 이 진 호

이 논문을 이학박사 학위논문으로 제출함
2020년 7월

서울대학교 대학원
물리천문학부
김 재 준

김재준의 이학박사 학위논문을 인준함
2020년 7월

위 원 장 김 창 영 (인)

부위원장 이 진 호 (인)

위 원 김 기 훈 (인)

위 원 양 범 정 (인)

위 원 심 지 훈 (인)

Abstract

After the discovery of the first Fe-based superconductor in 2006, several different types of Fe-based superconductors are synthesized and theoretical and experimental efforts were devoted to understand the mechanism of superconductivity. $Ca_{0.9}La_{0.1}FeAs_2$ was first synthesized in 2013 and attracted attentions of many theoretical researchers due to its unique As zigzag chain layer which can induce a topological superconductor. To elucidate the existence of topologically non-trivial property in this material, spectroscopic study is urgent. While Angle-Resolved PhotoEmission Spectroscopy (ARPES) results on $Ca_{0.9}La_{0.1}FeAs_2$ were reported, there is no Scanning Tunneling Microscope (STM) result so far.

In this thesis, the first STM result on $Ca_{0.9}La_{0.1}FeAs_2$ will be discussed in detail. All four types of different terminating layer were identified by analyzing topographic images, differential conductance maps, as well as spectral features. Each terminating layer exhibits a distinctive spectroscopic character. A nematic feature was observed on FeAs layer which has d_{xz} and d_{yz} orbital character. Ca layer above As zigzag chain layer shows an inhomogeneity in gap distribution and conductance map revealed an influence from La dopants on the underlying Ca layer. Cross-correlation analysis seems to suggest that the local superconductivity is disturbed by La dopants. Ca terminating layer above FeAs layer contained many crevices through which we could directly access the FeAs layer revealing a clear gap with coherence peaks. On As zigzag chain layer, our Fourier analysis revealed a Dirac-cone dispersion which is compatible with the previous ARPES results. Remarkably, many zero bias conductance peaks were observed on As zigzag chain layer especially only on top of the crevices of underlying Ca layer. The existence of zero bias conductance peak on As chain layer might provide a clue to verifying if $Ca_{0.9}La_{0.1}FeAs_2$ is topologically non-trivial superconductor. We hope our study opens a gate to a new direction in the study of this

fascinating material.

Keyword : Fe based superconductor, Scanning Tunneling Microscopy, Zero bias conductance peak, Nematicity

Student Number : 2013-20362

Table of Contents

List of Figures and Tables

Chapter 1. Introduction on Scanning Tunneling Microscope

After the invention of the scanning tunneling microscope (STM) in 1982 by Gerd Binning and Heinrich Rohrer [1], STM became a key experimental technique in condensed matter physics and other various fields. Extremely high resolution of STM is due to the fact that the tunneling current depends exponentially on the distance between an STM tip and a sample. To achieve such a high resolution, minimization of the vibration as well as the acoustic noise is a prerequisite. Low temperature and high vacuum also lower the noise. In this thesis, all STM experiments were performed at 4.2 K using a cryogenic high vacuum. In this chapter, I will explain briefly on the STM and the system we used.

1.1. Tunneling current and differential conductance

The schematic diagram to explain the tunneling effect in the STM is in figure 1.1. V is the bias voltage applied to the sample and φ is the work function. Normally, φ is ~ 5 eV and the applied voltage normally used is less than 0.5 V therefore we can make as an assumption that $\varphi \gg eV$. With that assumption, the probability of tunneling through energy wall height φ and width z is proportional to $e^{-2\frac{\sqrt{2m\varphi}}{\hbar}z}$. The tunneling current of the STM has an exponential dependence on the tip−sample distance. That exponential dependence is a key to the high spatial resolution of the STM.

Let's think the tunneling current in another way. The probability of transition from state μ to ν can be written as follows.

$$P_{\mu\nu} = \frac{2\pi}{\hbar}|M_{\mu\nu}|^2 \delta(E_\mu - E_\nu). \quad (1.1)$$

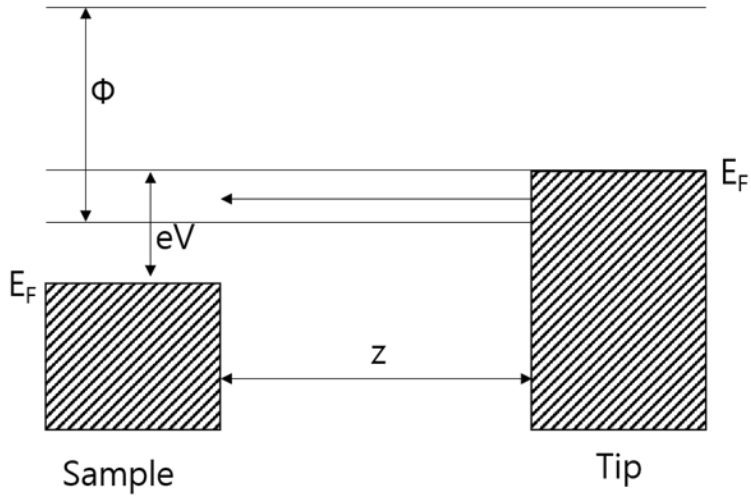

Figure 1.1 Schematic diagram of tunneling.

V is applied voltage to the sample, φ is work function and z is distance between tip and sample.

$M_{\mu\nu}$ is Bardeen's tunneling matrix element [2].

$$M_{\mu\nu} = \frac{\hbar^2}{2m}\iint \psi_\mu \frac{\partial \chi_\nu^*}{\partial z} - \chi_\nu^* \frac{\partial \psi_\mu}{\partial z} dxdy \tag{1.2}$$

When bias voltage V is applied to the sample, the total tunneling current is then

$$-2e\frac{2\pi}{\hbar}\int_{-\infty}^{\infty}\big[|M|^2\rho_{sample}(E)FD(E)\rho_{tip}(E-eV)\big(1-FD(E-eV)\big) - |M|^2\rho_{sample}(E)\big(1-FD(E)\big)\rho_{tip}(E-eV)FD(E-eV)\big]dE. \tag{1.3}$$

FD(E) is the Fermi Dirac distribution function,

$$\mathrm{FD(E)} = \frac{1}{1+e^{\frac{E}{k_B T}}} \tag{1.4}$$

By assuming almost zero temperature and $|M|^2$ is almost static in energy, the current can be rewritten as

$$\mathrm{I} = -\frac{4\pi e}{\hbar}|M|^2 \int_0^{eV}\left[\rho_{sample}(E)\rho_{tip}(E-eV)\right]dE. \tag{1.5}$$

Materials of the STM tip have an almost constant density of states around the Fermi energy normally. With the assumption of the constant density of state of the tip, the tunneling current is

$$\mathrm{I} = -\frac{4\pi e}{\hbar}|M|^2\rho_{tip} \int_0^{eV}\left[\rho_{sample}(E)\right]dE. \tag{1.6}$$

By differentiating the tunneling current I by applied voltage V,

$$\frac{dI}{dV} = -\frac{4\pi e^2}{\hbar}|M|^2\rho_{tip}\rho_{sample}(eV). \tag{1.7}$$

From the above equation, we can know that differential conductance is proportional to the local density of the state of the sample. Therefore, the measurement of the differential conductance by the STM is the key to investigate the electronic structure of the sample.

1.2. Topographic imaging

There are two different measurement types in the topographic image: a constant current mode and a constant height mode. In the constant current mode, to make the current constant, the tip moves ups and downs to compensate for the change of the current due to height change of a sample surface during the measurement. Measured z values give us the information on the surface. In the constant height mode, the tip's z value is fixed during the measurement, therefore the change of current gives us the information on the surface. The constant height mode is an indirect technic to measure z and there is always a possibility of collision between tip and sample. For those reasons, the constant current measurement is widely used these days. Figure 1.2 is an examples of a topographic image. Figure 1.2 is the topographic image of $Bi_2Sr_2CaCu_2O_{8+x}$ (100 nm x 100 nm size with 1200 x 1200 pixel resolution 200 mV/10 pA).

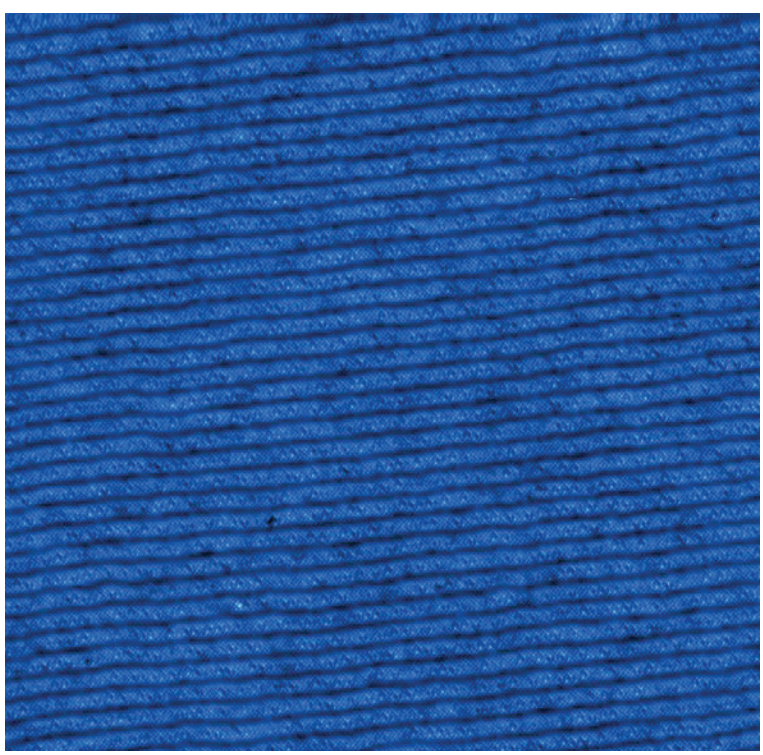

Figure 1.2 Topographic image of $Bi_2Sr_2CaCu_2O_{8+x}$.

1.3. Differential conductance spectroscopy and Spectroscopic Imaging Scanning Tunneling Microscopy

I−V and differential conductance spectra measurement is another important measurement of the STM experiment. I−V spectra can be measured by hold the position of the tip and measure the current during the sweep of bias voltage on samples. There are two methods to take the differential conductance: mathematical differentiation of measure I by voltage V and lock in technique. The mathematical differentiation is easy and straightforward but normally too noisy to use. The lock in technique is also easy but gives us a much clear result of the differential conductance. To get differential conductance spectra via the lock−in technique, one should apply a small modulation voltage with frequency ω during bias sweep. Using the Taylor expansion, the current can be written by,

$$\begin{aligned} &\mathrm{I}\left(\mathrm{V}_0 + \mathrm{V}_{\mathrm{mod}}\cos(\omega \mathrm{t} + \varphi)\right) \\ &= \mathrm{I}(V_0) + \frac{dI}{dV}|_{V=V_0} V_{mod}\cos(\omega \mathrm{t} + \varphi) + \ (higher\ \ order\ \ terms) \end{aligned} \tag{1.8}$$

By using the first harmonics measurement by a lock−in amplifier, we can measure the differential conductance without a numerical differentiation.

By measurement of spectra with a grid, it is possible to make a map of the differential conductance and the current with layers of energy. Differential conductance maps will be introduced after chapter 3.

1.4. Work function measurement and work function map

The relationship between the tunneling current and the tip-sample distance is discussed in section 1.1 and there is the work function φ. By measuring the change of the tunneling current and the tip-sample distance while x and y location of the tip is locked, the calculation of work function is possible using the following equation.

$$\varphi = \frac{\hbar^2}{8m}\frac{\Delta(\ln I)}{\Delta z} \tag{1.9}$$

Due to the resolution limit of the lock-in amplifier, the lock-in technique was not used to get the work function. By taking the I-z curve in the grid, it is possible to make a map of the work function.

1.5. Systems and equipment in Seoul National University.

This section covers the equipment in SNU thoroughly. Most of this section is published in [3].

1.5.1 Electronics

As described in section 1.2, for a topographic image, the constant current mode is used normally. To maintain the constant current above the sample surface, a control circuit of x, y, and z of the STM and the feedback circuit of tunneling current is essential. For that purpose, Nanonis™ BP4 was used. The tunneling current of my interest is less than 100 μA and normally order of 100 pA so amplification is essential. DLPCA-200 of FEMTO is used as a current amplifier. SR830 of Stanford Research Systems is for lock-in measurement and AH2550A of ANDEEN-HAGERLING is the capacitance bridge to measure the tip-sample distance via capacitance.

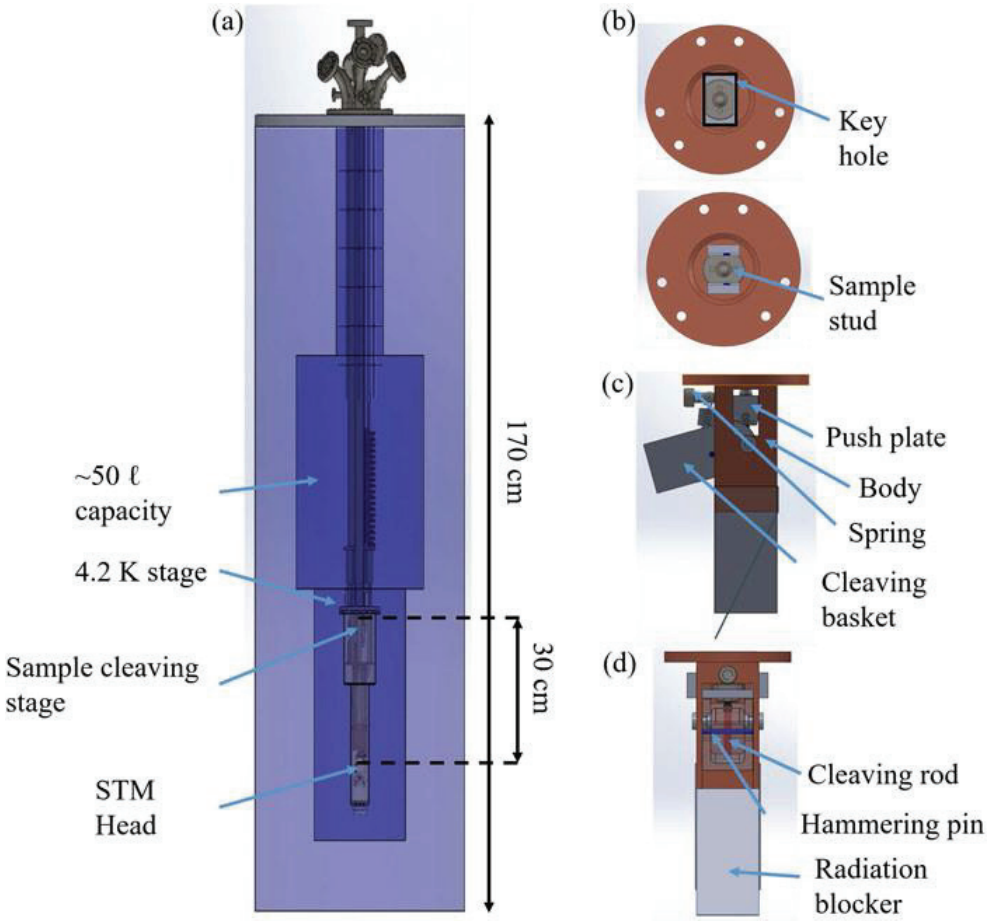

Figure 1.3 3D drawings of the cryostat, dewar and sample cleaving stage.

(a) 3D drawings of the cryostat and the Dewar. Location of the sample cleaving stage and the STM head is depicted. (b) Top view of the sample cleaving stage. The keyhole and a sample stud are shown. By rotating the sample stud, we can choose to pass it through the keyhole (upper figure) or stay on top of the keyhole (lower figure). ((c) and (d)) Side (c) and front (d) view of the sample cleaving stage. As the sample stud presses the push plate, the push plate forces the cleaving basket to rotate toward the body. The hammering pin is attached to the cleaving basket. Reproduced from [3], with the permission of AIP Publishing.

1.5.2 The cryostat and the Dewar

Figure 1.3 (a) is 3D drawings of the cryostat and the Dewar. The Dewar is 170 cm long and the storage size of useful liquid Helium is about 50 liters which can stand up to 8 days. The Dewar is from American Magnetics and 14 T magnet is located inside of the Dewar. The cryostat is homebuilt and there are 1 K pot and 300 mK pot to lower the temperature. 1 K pot is connected to a rotary pump and 300 mK is designed to have a charcoal pump inside.

1.5.3 Sample cleaving stage

Figure 1.3 (b) to (d) are 3D drawings of the sample cleaving stage. The brown parts are made of oxygen-free high thermal conductivity copper (OFHC) and other gray parts are made of 316 stainless steel. OFHC is selected because of a high thermal conductivity and 316 stainless steel is selected due to its strong property. The keyhole in figure 1.3 (b) is 90 degrees to the keyhole in the push plate of figure 1.3 (c). That 90-degree difference makes it possible to know where the sample is inside of the sample cleaving stage and also make sample stud to push the push plate to cleave the sample. The radiation blocker in figure 1.3 (d) is to block the radiation from the top of the cryostat.

Figure 1.4 (a) to (d) is a side view of the sample cleaving stage to explain the procedure of the sample cleaving process. The blue circle is hammering pin to hit sample cleaving rod (red) which is glued to sample surface. The sample stud is right on the push plate without pushing it. As sample stud start push the push plate, sample cleaving basket moves to the inward direction and also hammering pin (figure 1.4 (c)). When the push plate is fully pushed by sample stud, the hammering pin hit the sample cleaving rod and the sample cleaving process is over (figure 1.7 (d)). After that sample stud is rotated 90 degrees to go through push plate. After rotation, due to stretched coil spring, the cleaving basket moves to its original position.

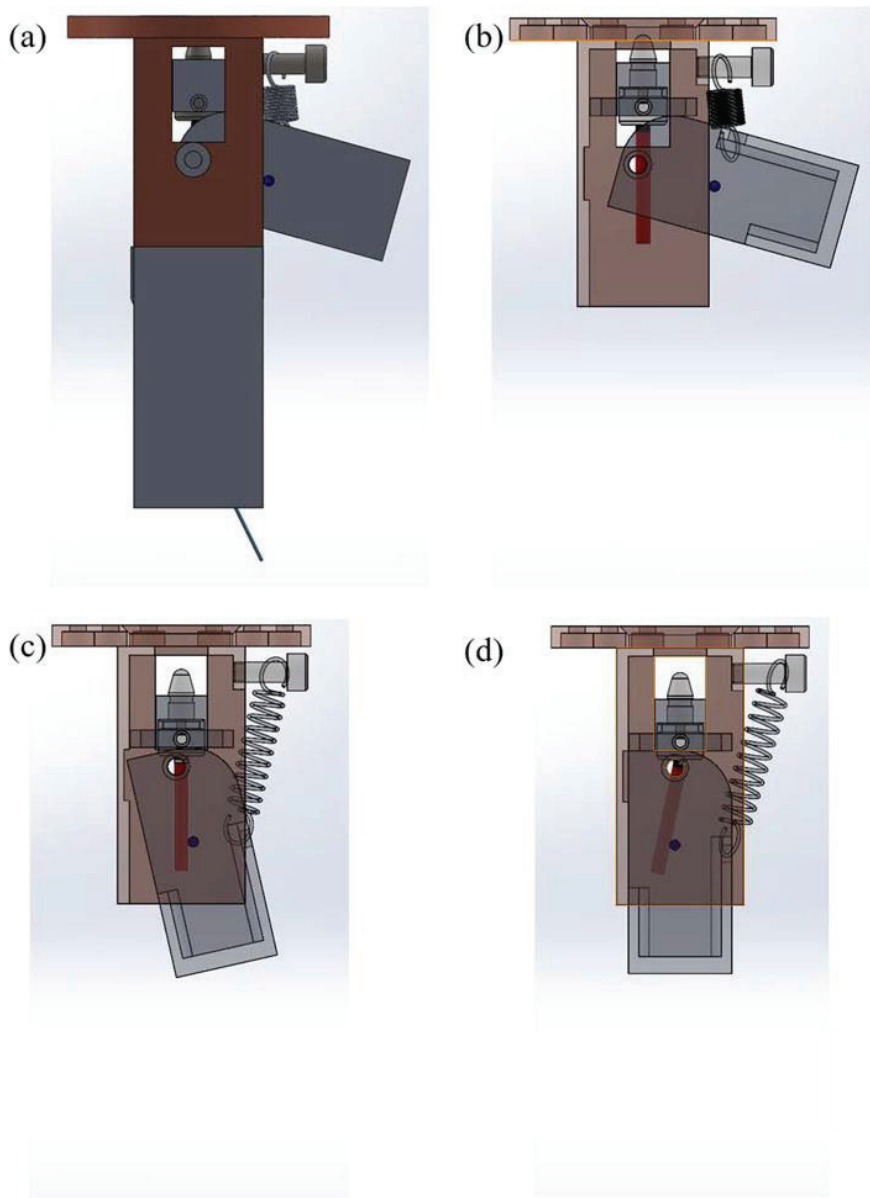

Figure 1.4 The movement illustration of sample cleaving stage.

(a) Side view of the cleaving system with the sample stud, sample, and cleaving rod. (b) Translucent view before the sample stud presses the push plate. (c) As the sample stud presses the push plate, the hammering pin (blue dot) attached to the cleaving basket starts to hit the cleaving rod (red rod) that is attached to the sample. (d) When the push plate is completely pressed down, the hammering pin knocks off the cleaving rod. Reproduced from [3], with the permission of AIP Publishing.

1.5.4 STM haed with tip treatment stage

The design of the STM head is based on a typical Pan style design [4]. But there is one most different thing from other STM head which is rotation plate used for tip treatment stage. The top view of the STM head and 3D drawings of tip treatment stage is in figure 1.5. Figure 1.5 (a) and (b) is the picture of STM head from the top with the gold is out of the tip position and on the tip position. The red line is to show the location of the gold target. The pictures are taken before the installation of the gold target. Figure 1.5 (c) is 3D drawings of figure 1.5 (a) and (b) without the top plate of STM head to see inside of the STM head. The upper image of figure 1.5 (c) is when the gold target is out of the tip position. STM tip can be seen fully from the top. The lower image of figure 1.5 (c) is when the gold target is on top of the tip. At that position, it is possible to tip treatment (field emission) on the gold target. Figure 1.5 (d) is a side view of the STM head especially tip treatment stage. Two sets of piezoelectric shear stacks are below and above the Sapphire plate. By pivot point in figure 1.5 (c), linear motion of piezoelectric shear stacks convert to rotational motion and make the sapphire plate to rotate. Lower piezoelectric shear stacks are glued to the body of the STM head. Upper piezoelectric shear stacks are lying above the sapphire plate without glue. The pressure is applied by ruby balls through spring by using tightening level of bolt on top of spring. If the pressure is too weak or too strong, the sapphire plate will not rotate. The rotation of the sapphire plate takes about 5 minutes with a bias voltage of 280 V. It can be changed by applied voltage on piezoelectric shear stacks and also by pressure through ruby balls on piezoelectric shear stacks.

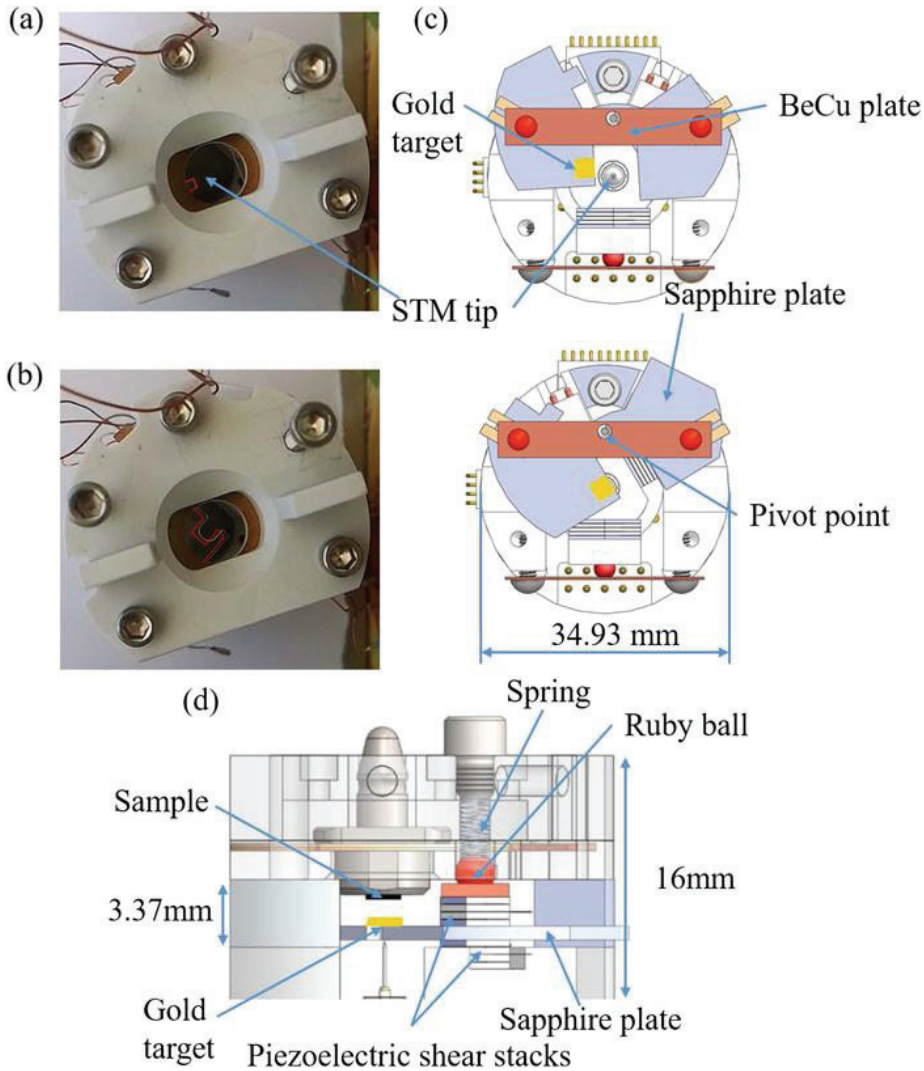

Figure 1.5 Top view of STM head and illustration of tip treatment stage.

Top view of the STM head. When the gold target is (a) out of the tip position and (b) on the tip position. Red lines show the location of the gold target. The gold target is not installed on the sapphire plate in these pictures. (c) Top view of the STM head with top parts removed for more clarity. (d) Side view of the STM head. There are two pairs of piezoelectric shear stacks above and below the sapphire plate. A pair of the piezoelectric shear stacks is attached to the STM head body and another pair of the piezoelectric shear stacks is attached to the BeCu plate and pressed by the BeCu plate, ruby balls, springs, and bolts. Reproduced from [3], with the permission of AIP Publishing.

1.5.5 Ultra low vibration system

3D drawings of the STM laboratory in Seoul national university is in figure 1.6. Tip-sample distance in STM measurement is the order of a nanometer, it is very important to make STM laboratory vibration isolated. For that purpose, high-density concrete used in the concrete block (figure 1. 6 (6)) to increase mass. Six air springs (figure 1.6 (8)) are placed bellow concrete block to minimize the vibration from outside. Due to the base design of the building, it is not possible to make a large space for one STM system. Therefore, efficient use of space is needed and concrete base design (figure 1.6 (7)) is the key to resolve that issue. Normal STM lab can contact air springs from outside of the concrete base but in this case, the concrete base is designed differently from other laboratories therefore air spring is possible to maintain from inside of the concrete base and save lots of space. The STM system is surrounded by the acoustic room (figure 1.6 (3)) to protect from the noise outside of the system. Three small air springs (figure 1.6 (5)) support the main table to minimize vibration maximally.

Figure 1.7 is the result of velocity spectral density measurement. The black curve is vibration measure from outside of the STM measurement system and the blue curve is inside of STM measurement system with full vibration isolation. In frequency around 300 Hz, vibration is suppressed about 1/100.

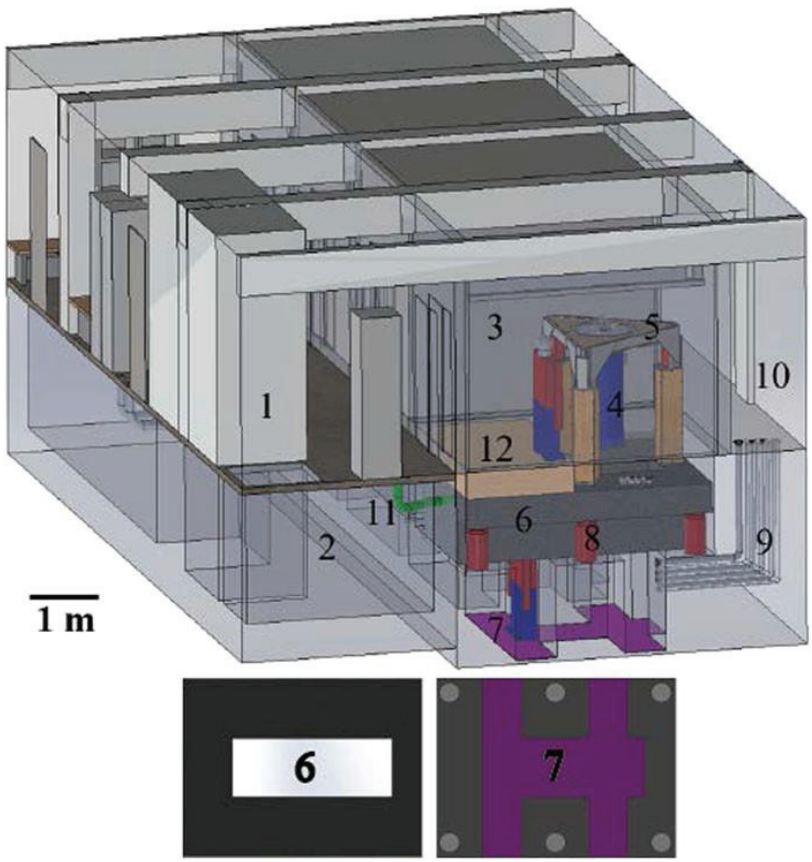

Figure 1.6 Schematic diagram of the SNU STM laboratory.

STM can be controlled from the control room (1). Space for the sample preparation (2). Inside the acoustic room (3), a cryostat and a Dewar (4) are mounted on the main table (5) which is supported by three air springs that are installed on top of the legs. The acoustic room is installed on top of the inertia block (6). The inertia block is on top of the concrete base (7) and six air springs (8) on the concrete base support the inertia blocks. Pump lines (9) are buried in the inertia block and base. They are connected to the pump room (10). The signal lines are extended to control the STM through PVC pipes (11) buried in the inertia blocks. To overcome the low-level ceiling, the acoustic room has a floor level lower than that of the control room. To resolve this problem, a false floor (12) is installed on top of the inertia blocks. Top views of the inertia block (6) and the concrete base (7) are also shown for clarity. Reproduced from [3], with the permission of AIP Publishing.

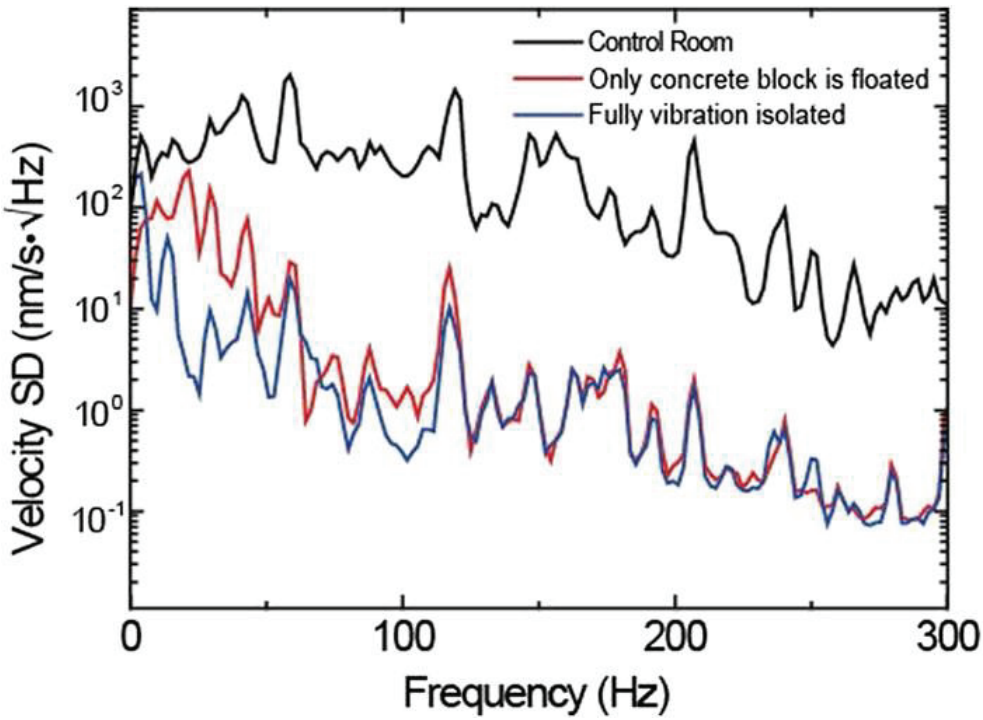

Figure 1.7 The result of vibration isoaltion system.

Velocity spectral density, measured by an OYO Geospace GEO-GS-11D, is plotted. The black curve shows the vibration noise measured in the control room. Inside the acoustic room, the geophone was installed on top of the main table. When the air springs supporting the inertia block is inflated (red curve) and all the vibration isolation system is activated (blue curve), vibration noise at all frequencies is highly suppressed. Reproduced from [3], with the permission of AIP Publishing.

Chapter 2. Introduction of Superconductivity and $Ca_{0.9}La_{0.1}FeAs_2$

2.1. Brief history of superconductor.

Onnes succeeded in the liquefaction of Helium in 1908. Using liquid Helium he discovered that rapid drop of conductivity below a certain temperature on Mercury [5]. That is the first observation of superconductivity in human history and that rapid conductivity drop temperature is the critical temperature of superconductor.

In 1933, Meissner and Ochesenfeld found another property of superconductor which is called perfect diamagnetism [6].

London equations [7] and Ginzburg–Landau theory [8] helps a lot for explaining of phenomena on superconductivity. In 1957 Bardeen, Cooper, and Schrieffer explained the superconductivity by their Bardeen–Cooper–Schrieffer theory [9].

Experimental research was also performed by many researchers to increase the critical temperature of superconductors, but before 1986, the critical temperature did not pass the walls of 30 K. In 1986, Bednorz and Müller discovered the lanthanum barium copper oxide which has a critical temperature 35 K which broke the walls of 30 K [10]. Also that is superconductor of a new type of family called cuprate superconductor which shares a common CuO_2 layer. After that, in 1987 $YBa_2Cu_3O_{7-x}$ was discovered which has a critical temperature of 93 K that exceeds the liquid nitrogen temperature (77 K) [11]. In 1988, $Bi_2Sr_2CaCu_2O_{8+x}$ was discovered which also has the critical temperature above liquid nitrogen temperature [12]. The highest critical temperature (in ambient pressure) of this cuprate superconductor family is 133 K in the Hg–Ba–Ca–Cu–O system [13].

In 2006, the first Fe-based superconductor was discovered in LaOFeP which has a critical temperature ~4 K [14]. The known highest critical temperature in Fe based superconductor is FeSe monolayer on $SrTiO_3$ [15] which has a critical temperature above 100 K.

After that, the sulfur hydride system showed a critical temperature at 203K at high pressure [16]. Recently, in 2019, the critical temperature reached ~250 K at 150 GPa on LaH_{10} which is very close to 273 K [17]. Figure 2.1 is the history of the critical temperature of superconductor.

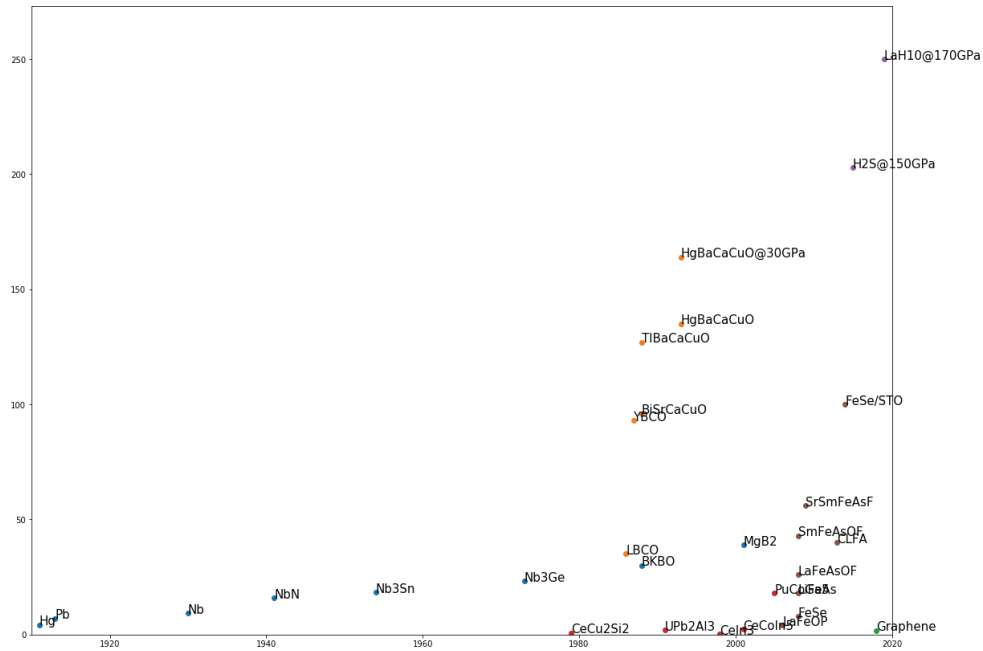

Figure 2.1 History of critical temperature of superconductor.

2.2. Fe-Based superconductors

LaOFFeAs, which was discovered after two years of the first discovery of iron based superconductor, attracted lots of interest due to its relatively high critical temperature 26 K [18]. After that, many different types of Fe-based superconductor has synthesized. Structure of each types of families are different but they have common FeX layer. X can be pnictogen (P, As) or chalcogen (S, Se, Te). The different types of families has different spacer layer which is located between FeX layers. The example of known types are 11(no spacer layer) (FeSe [19], FeTe [20] and FeS [21]), 111(LiFeAs [22], NaFeAs [23] and LiFeP [24]), 122($Ba_{1-x}K_xFe_2As_2$ [25], $(Ca_{1-x}Na_x)Fe2As2$ [26], $(K_{1-x}Sr_x)Fe2As2$ [27] and $(Cs_{1-x}Sr_x)Fe2As2$ [27]), 1111(LaOFeP [14], $SmFeAsO_{1-x}F_x$ [28], $CeO_{1-x}F_xFeAs$ [29], $Pr[O_{1-x}F_x]FeAs$ [30], $Nd[O_{1-x}F_x]FeAs$ [31], TbFeAs(O,F) [32] and DyFeAs(O,F) [32]), 32522($Sr_3Sc_2Fe_2As_2O_5$ [33]), 42622($(Fe_2P_2)(Sr_4Sc_2O_6)$ [34]), 21311(Sr_2VO_3FeAs [35]) and 112($Ca_{1-x}La_xFeAs_2$ [36], (Ca,Pr)$FeAs_2$ [37] and $Eu_{1-x}La_xFeAs_2$ [38]). The structure of those types are in figure 2.2 [39] (11, 111, 122, 1111, 32522), figure 2.3 (42622) [40] and figure 2.4 (112).

That many numbers of different types of Fe-based superconductors with different spacer layers can give a possibility of modifying the superconducting properties by the change of the spacer layer.

Figure 2.5 is FeAs lattice and 1-Fe and 2-Fe unit cell Brillouin zone [41]. Lots of Fe based superconductor shows similar features in the Fermi surface of 2-Fe unit cell Brillouin zone, which is the hole pocket around Γ and electron pocket around M (figure 2.5 (c)).

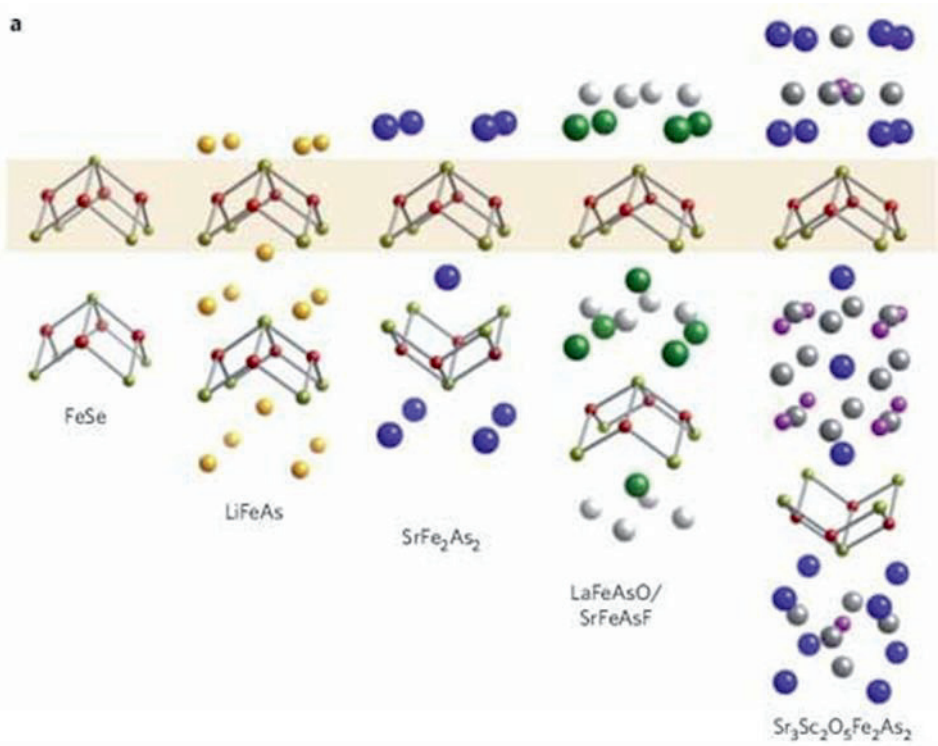

Figure 2.2 Structure of 11, 111, 122, 1111 and 32522 Fe based superconductors.

Lattice structure of 11, 111, 122, 1111 and 32522 Fe-based superconductors. Reprinted by permission from Springer Nature Customer Service Centre GmbH: Springer Nature. Nature Physics, High-temperature superconductivity in iron-based materials, Paglione, J., Greene, R. [39], ⓒ 2010

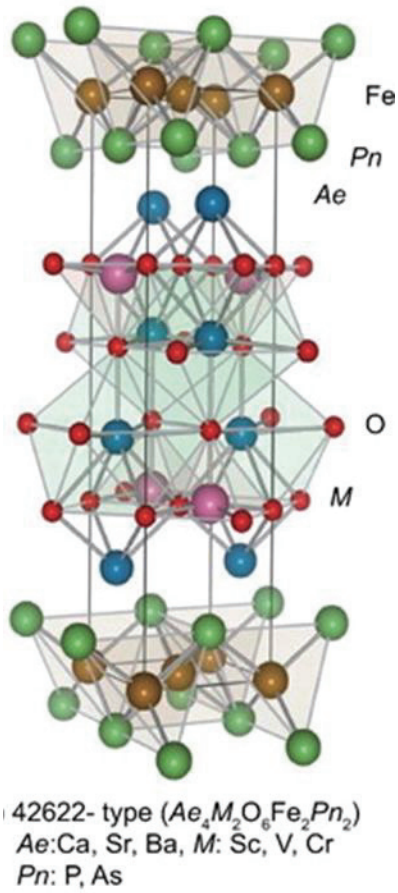

Figure 2.3 Crystal structure of 42622 Fe based superconductor.

The lattice structure of 42622 Fe based superconductors. Reproduce from [40].

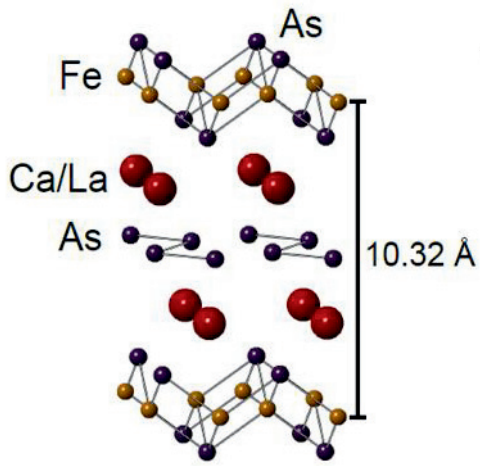

Figure 2.4 Crystal structure of 112 Fe based superconductor.

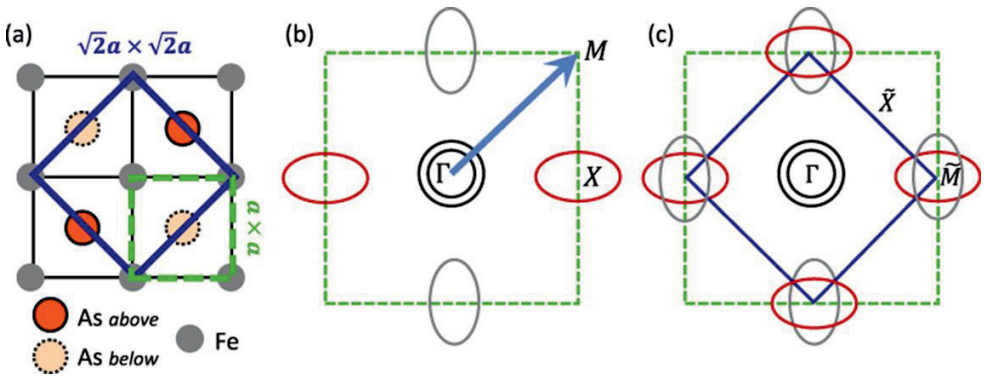

Figure 2.5 FeAs lattice and Fermi surfaces.

(a) FeAs lattice. Blue box is the 2−Fe unit cell and green dashed box is the 1−Fe unit cell lattice. (b) The fermi surface of the 1−Fe Brillouin zone. (c) The 2−Fe Brillouin zone is indicated by the blue box [41].

2.3. $Ca_{0.9}La_{0.1}FeAs_2$

$Ca_{0.9}La_{0.1}FeAs_2$ is recently synthesized material [36] which has some special properties compared to other types of Fe based superconductors. First is it has a monoclinic crystal structure. Normally other types of Fe based superconductor has an orthorhombic or tetragonal structure. Second is it has an As zigzag chain layer as a part of the spacer layer. As zigzag china layer is observed by synchrotron X-ray diffraction analysis [36]. The third is noncentrosymmetric. The other samples such as $Eu_{1-x}La_xFeAs_2$ [38] and $(Ca,Pr)FeAs_2$ [37] have the monoclinic but centrosymmetric structure. The noncentrosymmetric structure of $Ca_{0.9}La_{0.1}FeAs_2$ is confirmed by a rotational anisotropy second harmonic generation [42]. It has an antiferromagnetic property similar to 122 material. In one direction Fe atoms aligned to be antiferromagnetic and in other direction aligned to have ferromagnetic (figure 2.6) [43] .

Due to its noncentrosymmetric property, it can be one candidate of a topological superconductor. Sato and Fujimoto showed the possibility of the topological phase in the noncentrosymmetric superconductor [44].

Wu *et al.* claimed that due to the spin-orbit coupling by La dopants in $Ca_{0.9}La_{0.1}FeAs_2$, As zigzag chain layer can be a topological insulator in some cases. Also, they claimed the possibility of a one-dimensional topological superconductor in $Ca_{0.9}La_{0.1}FeAs_2$ [45].

Due to the existence of As zigzag chain layer in $Ca_{0.9}La_{0.1}FeAs_2$, an electron pocket around X exist (figure 2.7) which are absent in other types of Fe-based superconductor and that band is measured by Angle-Resolved Photo Emission Spectroscopy (ARPES) [46].

$Ca_{0.9}La_{0.1}FeAs_2$ and $CaFe_2As_2$ have a similar chemical formula and some of layers are same between them. From the comparison between figure 2.2 and figure 2.4, it is easy to notice that FeAs layer and Ca layer above FeAs layer is same. But, in the case of the $Ca_{0.9}La_{0.1}FeAs_2$, it has two more layers between FeAs layers. One is As zigzag chain layer and the other is Ca layer above FeAs layer. Due to those two layers, unlike the 122 material, the possible terminated layer is four.

Figure 2.8 is TEM data of $(Ca,Pr)FeAs_2$ [37]. From the figure, the distance between Ca layer and As zigzag chain layer looks larger than the distance between Ca layer and FeAs layer so Ca and As zigzag chain layers might be easily terminated surface.

In remaining chapters, I will discuss the STM data of $Ca_{0.9}La_{0.1}FeAs_2$ which has Tc ~ 40 K. STM measurement was peformed at the temperature of 4.2 K with the high vacuum. Luckily, all four possible layers were observed and identification of surfaces will be discussed later.

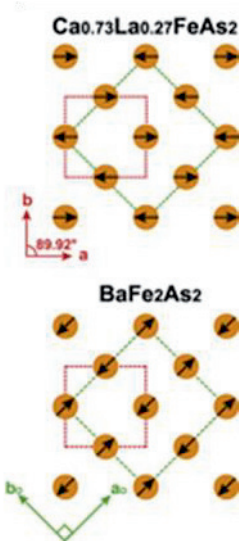

Figure 2.6 Antiferromagnetic structure of 112 and 122.

Antiferromagnetic structures of $Ca_{0.73}La_{0.27}FeAs_2$ and $BaFe_2As_2$ [43]. © IOP Publishing. Reproduced with permission. All rights reserved.

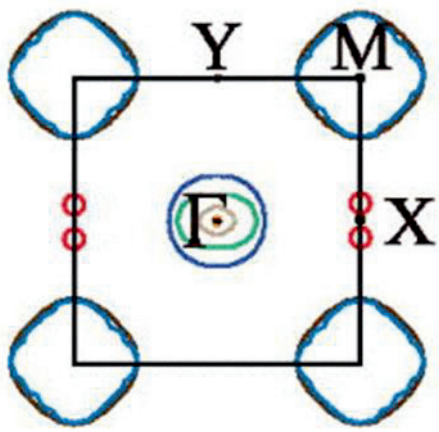

Figure 2.7 Calculated fermi surface of $Ca_{0.9}La_{0.1}FeAs_2$.

Calculated fermi surface of $Ca_{0.9}La_{0.1}FeAs_2$ of two Fe atom containing Brillouin zone. Two electron pockets are around X point. Reproduce from [46], with the permission of AIP Publishing.

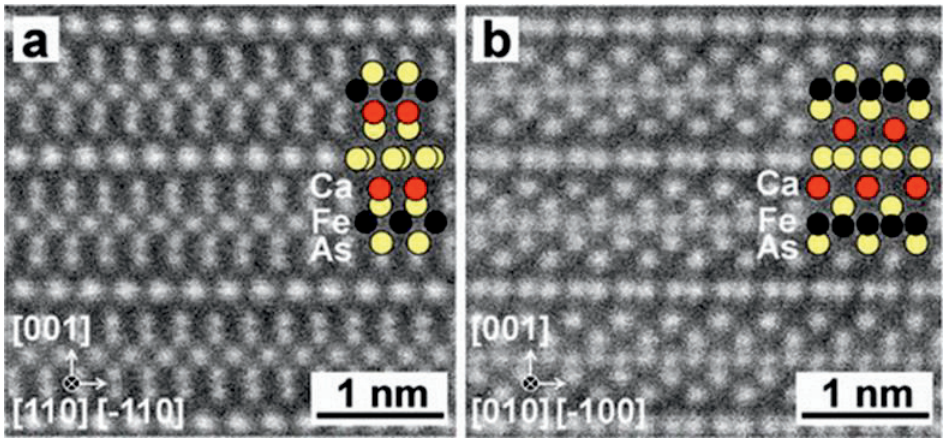

Figure 2.8 STEM image of (Ca,Pr)$FeAs_2$.

High-angle annular dark field scanning transmission electron microscope (STEM) image of the (Ca,Pr)$FeAs_2$ from (a) [110] direction (b) [010] direction. From the distance between layers, Ca layer or As zigzag chain layers seems easy to be terminated. Reprinted with permission from [37]. Copyright (2014) American Chemical Society.

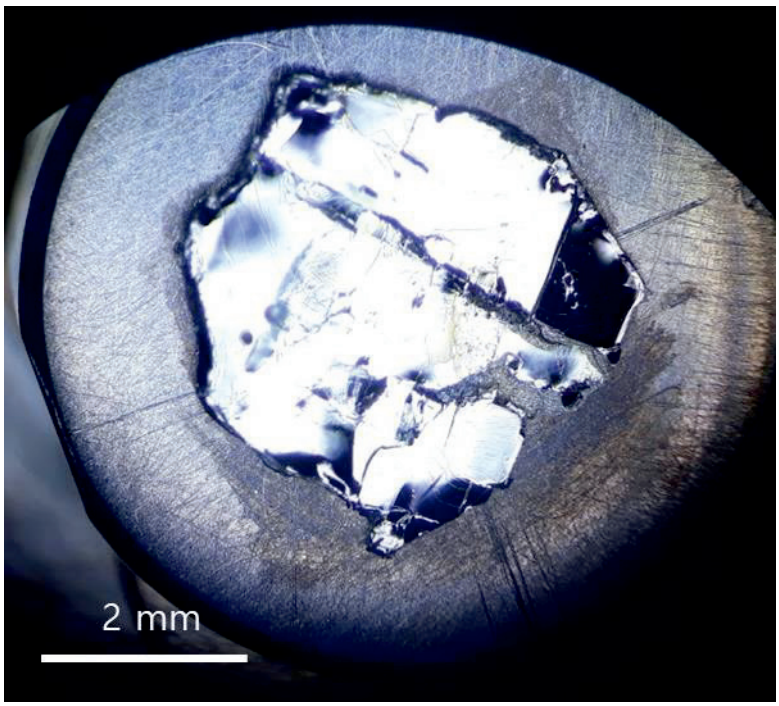

Figure 2.9 Picture of $Ca_{0.9}La_{0.1}FeAs_2$ sample after STM measurement.

Chapter 3. Nematic features on FeAs layer

3.1. Identification of FeAs layer.

$Ca_{0.9}La_{0.1}FeAs_2$ is a novel material and still, there are no published STM experiments yet. To identify the each surface, I compared the topographic image of $Ca_{0.9}La_{0.1}FeAs_2$ to that of Ca 122 [47] due to common layers between them. FeAs layer (figure 3.1) is an essential layer for a superconductivity, therefore, it is reasonable to predict that the superconducting spectrum is visible everywhere and according to the case of Ca 122 [47], the surface is predicted to show 2x1 surface reconstruction. Figure 3.2(a) is a topographic image taken on FeAs layer at 4.2 K. It shows the 2x1 surface reconstruction (figure 3.3) as expected. The averaged spectrum of the entire field of view of figure 3.2(a) is in figure 3.2(b) (black). The averaged spectrum shows superconducting features but particle-hole asymmetric and the center of the dip is slightly shifted to the positive side. That is due to FeAs layer is negatively charged. Known chemical formula $(Ca^{2+}_{1-x}La^{3+}_{x})(Fe^{2+}_{2}As^{3-}_{2})_{1/2}As^{-} \cdot xe^{-}$ [36] indicates that the surface could be negatively charged. Figure 3.4 is a schematic illustration of this situation. The surface is charged negatively (figure 3.4 (a)) so if there is no applied bias voltage on the sample holder, net bias voltage on the sample is slightly negative. To make the net bias voltage on the sample as zero, a slight positive bias applied to the sample holder is needed (figure 3.4 (b)). That is why the center of the superconducting spectrum shows the slight positive shift on the averaged spectrum (black line of figure 3.2(b)).

In the averaged spectrum (black line of figure 3.2(b), it is hard to define a coherence peak so determine the size of the gap is hard in the usual way. To overcome that problem and find the superconducting gap value, the numerical differentiation of dI/dV

(d^2I/dV^2) was used to find gap values. The averaged spectrum of d^2I/dV^2 is the blue line in figure 3.2(b). Compare to dI/dV (averaged spectrum, black), the peak is very sharp and easy to define in d^2I/dV^2. It is not a direct measurement of gap value,

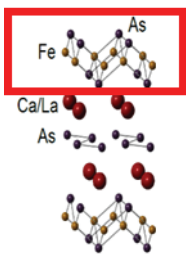

Figure 3.1 Crystal structure of $Ca_{0.9}La_{0.1}FeAs_2$ and FeAs layer.

Crystal structure of $Ca_{0.9}La_{0.1}FeAs_2$. FeAs layer is in red box.

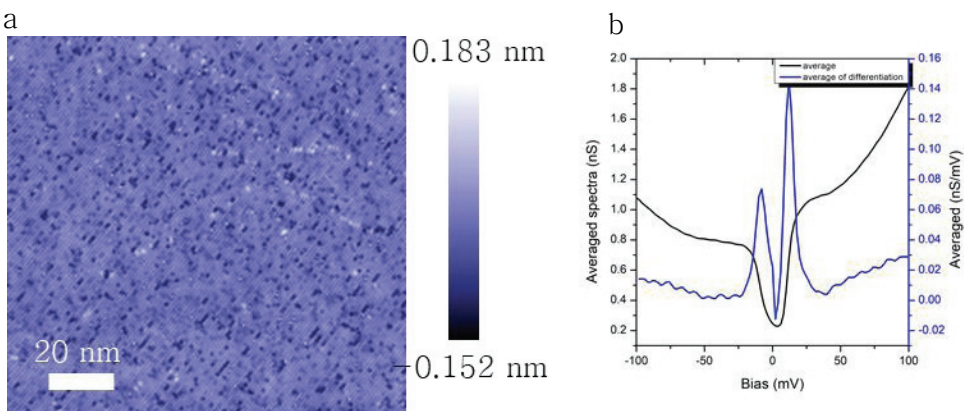

Figure 3.2 Topographic image and averaged spectra taken on FeAs layer.

(a) Topographic image(−100 mV/100 pA, 88 nm x 88 nm) of FeAs layer. (b) Averaged spectrum of conductance spectra (dI/dV) (black line) shows superconducting gap feature but no evident coherence peaks. Center of spectrum is shifted positively from zero bias. Averaged spectrum of derivative of conductance spectra (d^2I/dV^2) (blue line). Peak is evident in d^2I/dV^2.

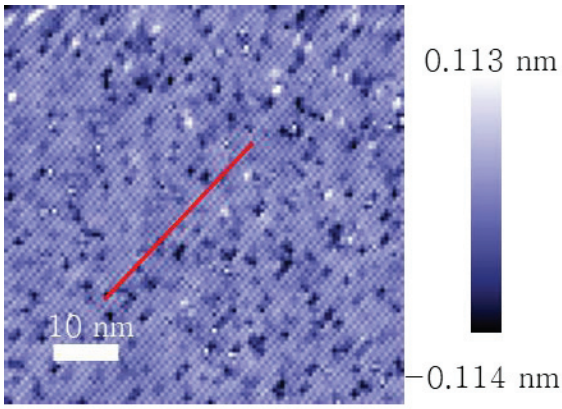

Figure 3.3 Zoomed in topographic image.

Upper left corner of topographic image of figure 3.2(a) (44 nm x 44 nm) to show 2x1 surface reconstruction more clearly. Red line is indication of 2x1 surface reconstruction direction.

so it is not appropriate to use this value as the absolute gap value but still, we can see the tendency and the distribution of the gap size of FeAs layer. Figure 3.5 is the gap map which is a visualization of the gap using gap values from d^2I/dV^2. It shows that gap values on FeAs layer have relatively homogeneous distribution. That is because this result was measured on FeAs layer. This layer can be concluded as the FeAs layer from the 2x1 reconstruction of the topographic image, positively shifted spectrum, and homogeneous gap distribution.

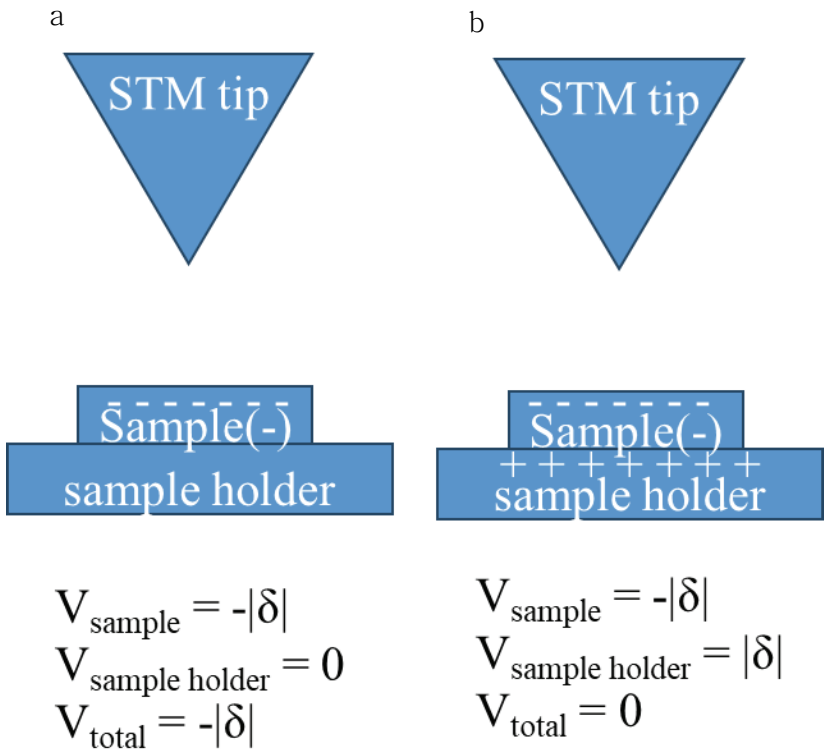

Figure 3.4 Illustration of charged surface effect.

Illustration of charged surface effect. (a) Sample is charged negatively and applied bias voltage on sample holder is zero. Net bias voltage on sample is slightly negative ($-|\delta|$) due to sample charge. (b) Sample is charged negatively and bias voltage is positive ($+|\delta|$). Net bias voltage is zero due to sample charge effect is compensated by applied bias voltage on sample holder.

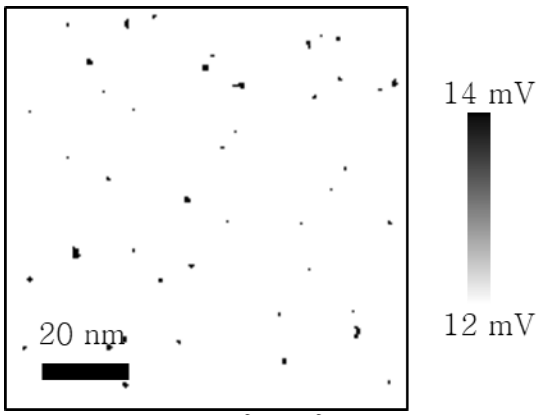

Figure 3.5 Gap map using numerical d^2I/dV^2 methodology.

Gap map using numerical d^2I/dV^2 methodology. It shows relatively homogeneous gap distribution.

3.2. Nematic features observed on FeAs layer.

Figure 3.6 are conductance maps taken above FeAs layer from bias voltage −30 mV to + 2 mV with a 4 mV difference. Nematic features elongated vertically were observed. Those features are visible at the bias voltage of −30 mV and weaken as the bias voltage increased to + 2mV. To identify the origin of those features and which band give those features, a Fourier transform was applied on those conductance maps. Figure 3.7 are the Fourier transform of figure 3.6. To enhance signals of the Fourier transform images, two enhancement processings were applied. First, the Fourier transform was applied on the conductance map after subtraction on a Gaussian averaged conductance map to minimize the central peak on Fourier transform image. Second, maps were rotated to make Bragg peaks on the 45−degree direction. After that maps were folded along horizontal and vertical which are along a−axis and b−axis of the crystal. The bright peaks right above and below of the center and two lines around center are by−products of those signal enhancement

process.

In Fourier transform images, there are bright peaks (q* in figure 3.7) in each energy along horizontally. As the bias voltage increases from −30 mV to 2 mV, those peaks move to the inward direction. To investigate that movement quantitatively, a line profile along the horizontal direction (blue arrow in figure 3.7) was taken and that line profile direction is $\Gamma - M$ direction in Fermi surface (figure 2.7) [46]. Due to the broad peak's width, the usual peak fitting function was not working well with the direct line profile (figure 3.8 (a)). To find the peak's center systemically, the amplitude of the gradient of figure 3.6 is calculated and the line profile (figure 3.8 (b)) was taken after that procedure. To find the peak's center is changed to find the new line profile's local minimum which is the original line profile's peak location. The result of those processes to find the peaks in figure 3.7 is in figure 3.9 (a). The dispersion curve clearly shows particle−hole asymmetric behavior and hole like dispersion character.

To find which band can give that dispersion behavior, comparison to an ARPES measurement is carried out. The peak's location by the STM result is q value, not k value. To match STM data to ARPES measurement, the conversion of q to k is essential. The q vector is nothing but the difference between two different k vectors. In this case, q is divided by 2 which means q vector is difference of two different k vector which has the same amplitude and opposite direction. The result of the comparison to ARPES measurement on $Ca_{0.9}La_{0.1}FeAs_2$ [48] is in figure 3.9 (b). The STM result (red dots) matches well to ζ band of the ARPES measurement both in size and angle. The energy of the STM result shifted around −70 meV. The doping level of the sample used in the STM and the ARPES measurement is same so it is expected to have no energy difference between those two results. That energy difference is due to the difference between the nominal doping level and the actual doping level.

The ζ band has the d_{xz} and d_{yz} orbital character. Those d_{xz} and d_{yz} orbitals are claimed to be the origin of nematicity in previous research on other samples [49,50].

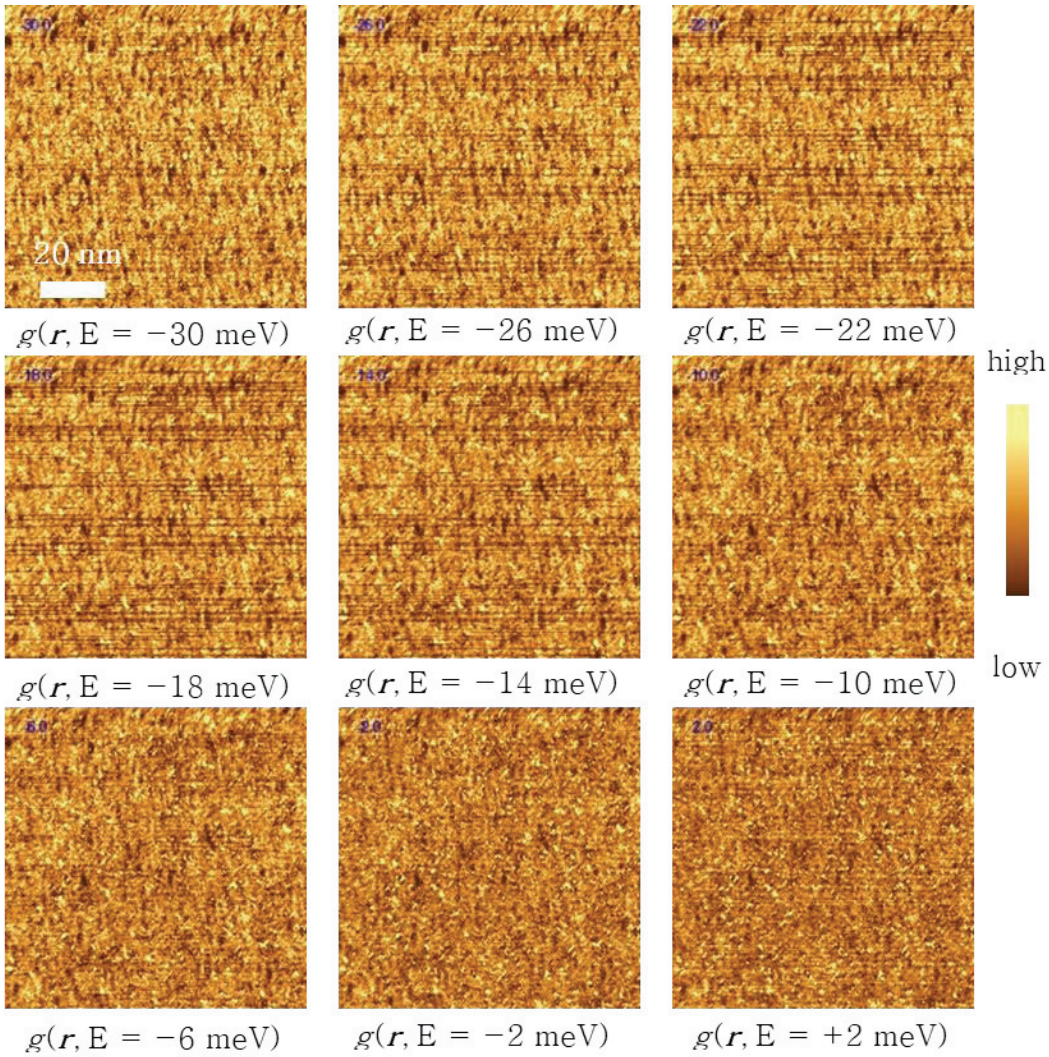

Figure 3.6 Conductance maps on Fe As layer.

Conductance maps simultaneously taken with topographic image (figure 3.2(a)) on FeAs layer with bias voltage from −30 mV to 2 mV with 4 mV difference. It shows vertically aligned neamtic features. The strength of nematic features are getting weaken as the bias voltage increases.

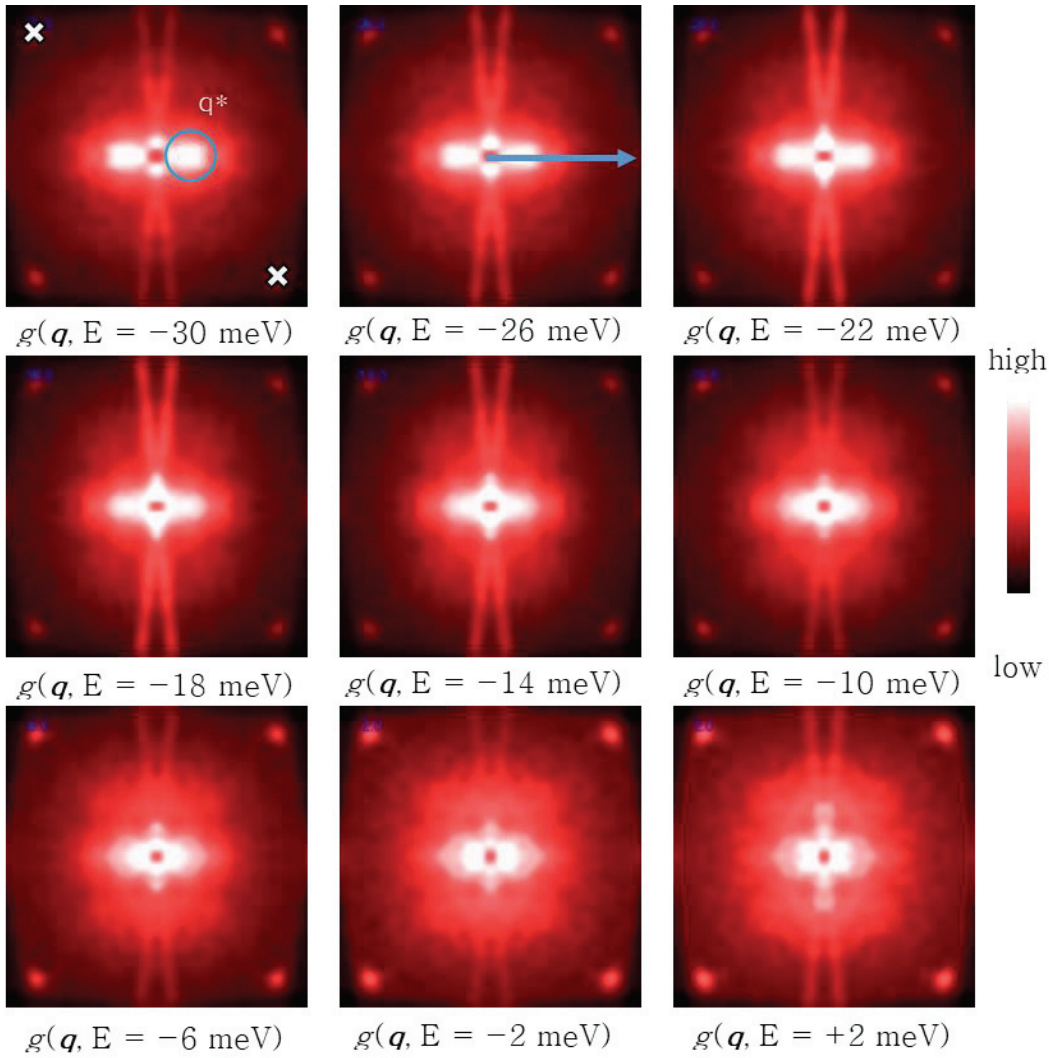

Figure 3.7 Fourier transform of conductance maps.

Fourier transform image of figure 3.5. Two x marked points in upper left and lower right corner are Bragg peaks point from 2x1 surface reconstruction. Two bright points in other corners are by-product of signal enhancement process. Bright peaks which located side of center (q*, blue circle) are moved inward as bias voltage increases. From this image, it is quite evident that q* shows hole like dispersion. Blue arrow indicates the line profile direction and it is $\Gamma - M$ direction of Fermi surface.

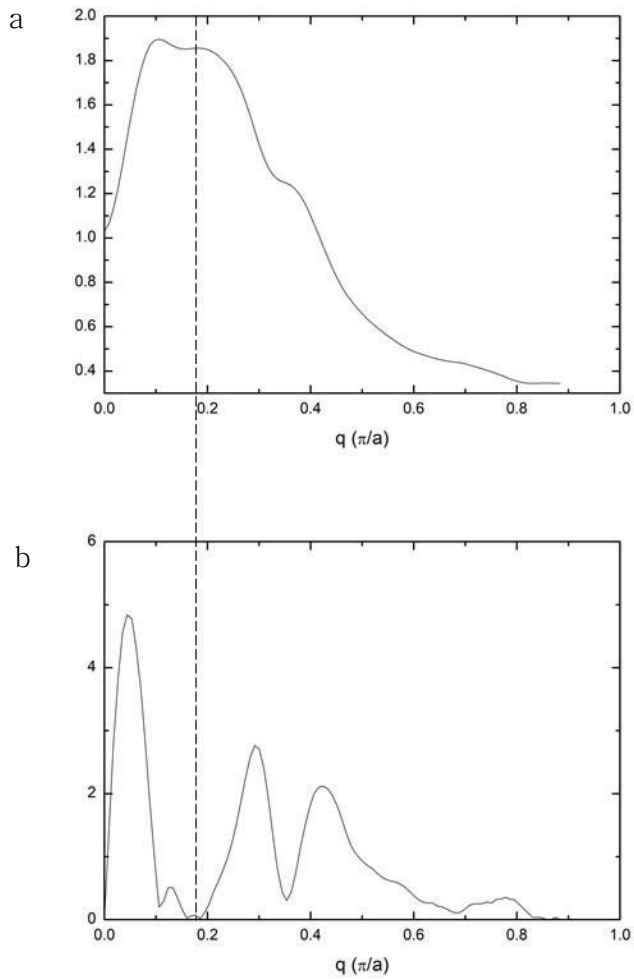

Figure 3.8 Line profile of Fourier transform of conductance map.

(a) Line profile of Fourier transform of conductance map at bias voltage of −30 mV. Due to broad peak, usual fitting function is not working well.

(b) Line profile of amplitude of gradient on Fourier transform of conductance map at bias voltage of −30 mV. From (a) to (b), it changed to find peak's local maxima to local minimum. Gaussian function with negative coefficient is working well in (b).

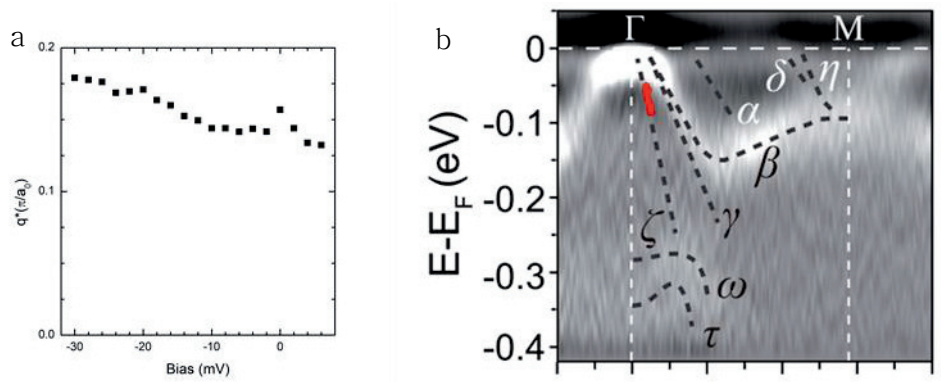

Figure 3.9 q* vs bias voltage plot and fit with ARPES measurement.

(a) Plot of the location of q* in figure 3.7 (using amplitude of gradient) versus bias voltage. It shows clear particle hole asymmetric and hole-like dispersion. (b) Comparison between STM result (red dots) and ARPES measurement (background). ARPES measurement was taken with circularly polarized photon with energy 104 eV at 15-20 K. Result of STM matches well with ζ band in ARPES measurement. Reproduced from [48]. Copyright 2015 by The American Physical Society.

3.3. Summary.

In this FeAs layer, the 2x1 surface reconstruction is observed in the topographic image. The gap map by numerical d^2I/dV^2 methodology shows the relatively homogenous distribution of gap values in the entire field of view. Nematic features are observed in the conductance map and from Fourier transform analysis, it shows clear hole like dispersion. The origin of nematic feature is ζ band which has d_{xz} and d_{yz} orbital character.

Chapter 4. Inhomogeneous gap distribution and underlying La dopants on Ca/La layer above As chain layer.

The Ca layer has only one type of possibility in $CaFe_2As_2$ material which is sandwiched by FeAs layers. Unlike the case of the $CaFe_2As_2$, there are two possibilities in $Ca_{0.9}La_{0.1}FeAs_2$. One is Ca/La layer with above As chain layer (Ca-1). The other is Ca/La layer above FeAs layer (Ca-2). Though two layers have same atoms, due to different underlying layers, there is a possibility that two layers can show different behavior. In this section, I will discuss the data taken above Ca-1 (figure 4.1).

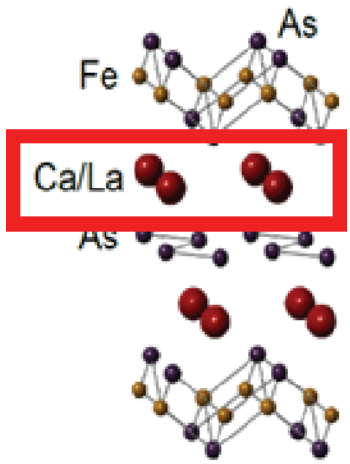

Figure 4.1 Crystal structure and Ca-1 layer.

The crystal structure of $Ca_{0.9}La_{0.1}FeAs_2$. The red box indicates Ca/La layer above As chain layer which is discussed in this chapter.

4.1. Identification of Ca/La layer above As chain layer.

Figure 4.2 (a) is a topographic image (92 nm x 92 nm, I = 150 pA and bias voltage = 150 mV) and it shows the 2x1 surface reconstruction (figure 4.3). Though there is no prediction in $Ca_{0.9}La_{0.1}FeAs_2$, Ca layer of the $CaFe_2As_2$ is predicted to have the 2x1 surface reconstruction by a theoretical calculation [51].

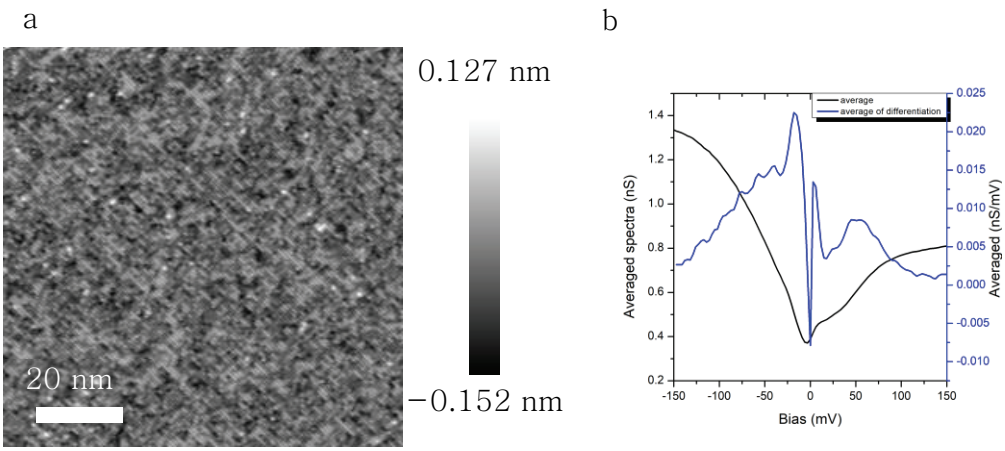

Figure 4.2 Topographic image and averaged spectra on Ca−1 layer.

(a) Topographic image (150 mV/ 150 pA) taken on Ca−1 layer. It shows 2x1 surface reconstruction (b) Averaged spectrum of conductance spectra (dI/dV) (black) shows superconducting gap feature around less than 20 mV but no evident coherence peaks. Center of spectrum is shifted negatively from zero bias. Averaged spectrum of derivative of conductance spectra (d^2I/dV^2) (blue) shows evident peak.

The black line in figure 4.2(b) is averaged spectrum taken on the entire field of view of figure 4.2(a). That spectrum shows the superconducting gap feature less than the bias voltage of around 20 mV. The center of the dip of the averaged spectrum is shifted to the negative side. From chemical formula and underneath layer, Ca−1

layer predicted as a positively charged surface. That positively charged surface effect on net bias voltage is illustrated in 4.4. Due to the positive charge on Ca−1 layer, the averaged spectrum shows the slight negative side shift in shape. From those two specific features of this layer, the measured layer can be concluded as Ca−1 layer.

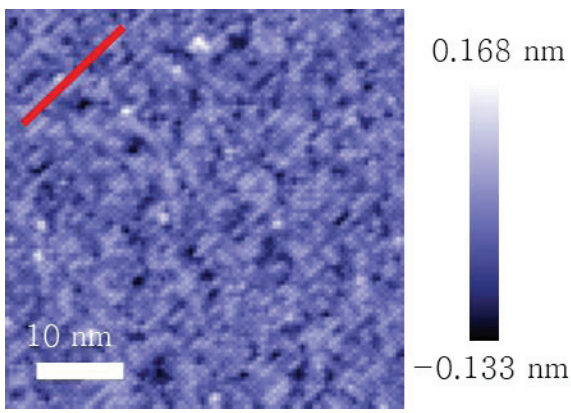

Figure 4.3 Zoomed in topographic image.

Zoomed in image of lower right corner in figure 4.2 (a). Size of field of view is 46 nm x 46 nm. Red line is indication for the 2x1 surface reconstruction direction.

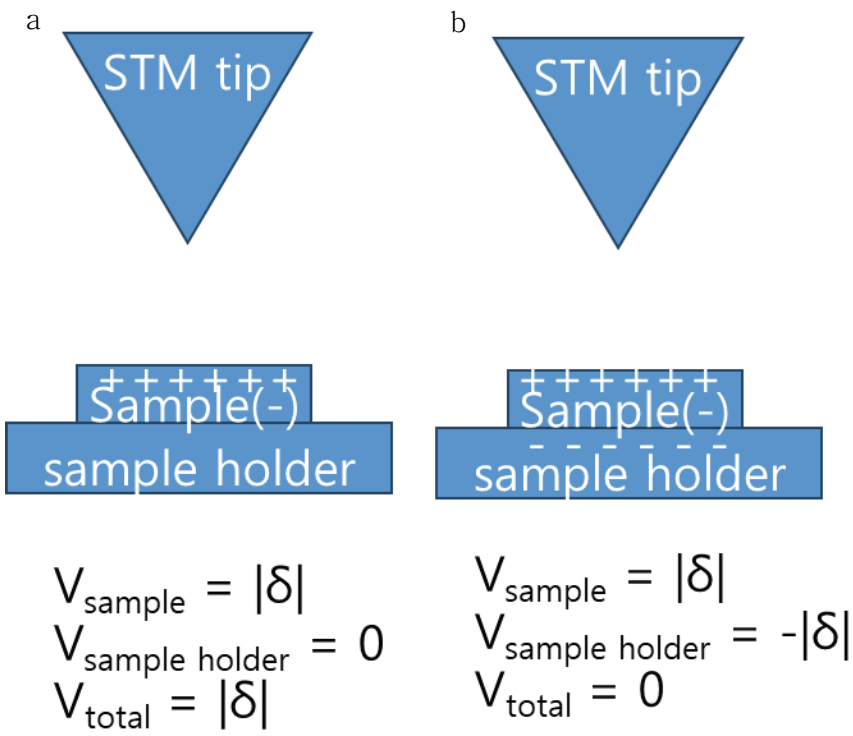

Figure 4.4 Illustration of charged surface effect.

Illustration of charged surface effect. This situation is opposite situation in FeAs layer (figure 3.4). (a) Sample is charged positively and applied bias voltage on sample holder is zero. Net bias voltage on sample is slightly positive ($|\delta|$) due to sample charge. (b) Sample is charged positively and applied bias voltage on sample holder is negative ($-|\delta|$). Net bias voltage is zero due to sample charge effect is compensated by applied bias voltage on sample holder.

4.2. Inhomogeneous gap distribution of Ca-1 layer.

The averaged spectrum (black curve in figure 4.2 (b)) shows a gap like V-shape dip around the center. Like the case of the FeAs layer (black curve in figure 3.2 (b)), the coherence peak is hard to define directly. The numerical calculation of d^2I/dV^2 methodology is used again to find gap values and investigate the distribution and tendency of those gaps. The blue curve in figure 3.2 (b) is averaged spectrum of numerical calculated d^2I/dV^2. It shows clear peaks around the center therefore it is easy to define gap values using d^2I/dV^2. As mentioned earlier, these values are not absolute values for the gap.

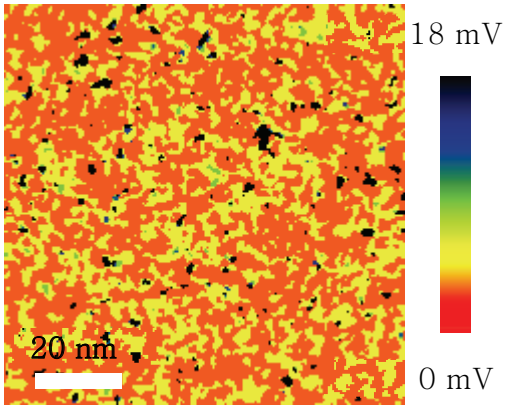

Figure 4.5 Gap map using numerical d^2I/dV^2.

The distribution of gap values of each points which are extracted from numerical d^2I/dV^2. It shows inhomogeneous distribution which is definitely different from the gap map of FeAs layer.

Figure 4.5 is the gap map which shows the distribution of gap values from numerical d^2I/dV^2. Unlike the gap map result of FeAs layer (figure 3.5), it shows evident inhomogeneous gap distribution. The gap histogram is in figure 4.6 (a). Most of the gap values are 3 meV and 6 meV. Figure 4.6 (b) is gap sorted spectra which is

averaged spectra of each gap value. From the gap value 3 meV to 15 meV, V-shaped dip shows increased as energy increased. The V-shaped dip feature disappears in averaged conductance spectrum of 18 mV bias voltage. From comparison to averaged spectra of other gap values, it is possible to say 18 meV gap value area is where superconductivity suppressed. Figure 4.7 (a) is a visualization of 18 meV gap value area. The white area is where superconductivity is suppressed. By comparing that to conductance maps of each energy, conductance maps at certain energy show very similar features with figure 4.7 (a).

To verify this claim, a cross-correlation of conductance maps of each energy and superconductivity suppressed area image (figure 4.7 (a)) is carried out. The result of the cross-correlation is in figure 4.7 (b). The cross-correlation coefficient has a peak at -12 mV. Figure 4.8 (a) is the conductance map at -12 mV bias voltage. Comparing those two images, the white features in each image seem to overlap considerably. Figure 4.8 (b) is the mask of the bright feature area in the conductance map (figure 4.8 (a)). Figure 4.9 (a) is the result of cross-correlation between figure 4.7 (a) and 4.8 (b). It shows a very rapid coefficient drop.

To see how rapidly the coefficient diminishes, the azimuthal averaged was applied on the cross-correlation map. Figure 4.9(b) is the result of the azimuthal average of figure 4.9 (a). The peak of cross-correlation coefficient is 0.268 at zero distance. As the distance increases, cross-correlation coefficient shows a rapid drop and it reaches zero around 2 nm which implies that the correlation between white features in the conductance map and superconductivity suppressed area is in a localized fashion.

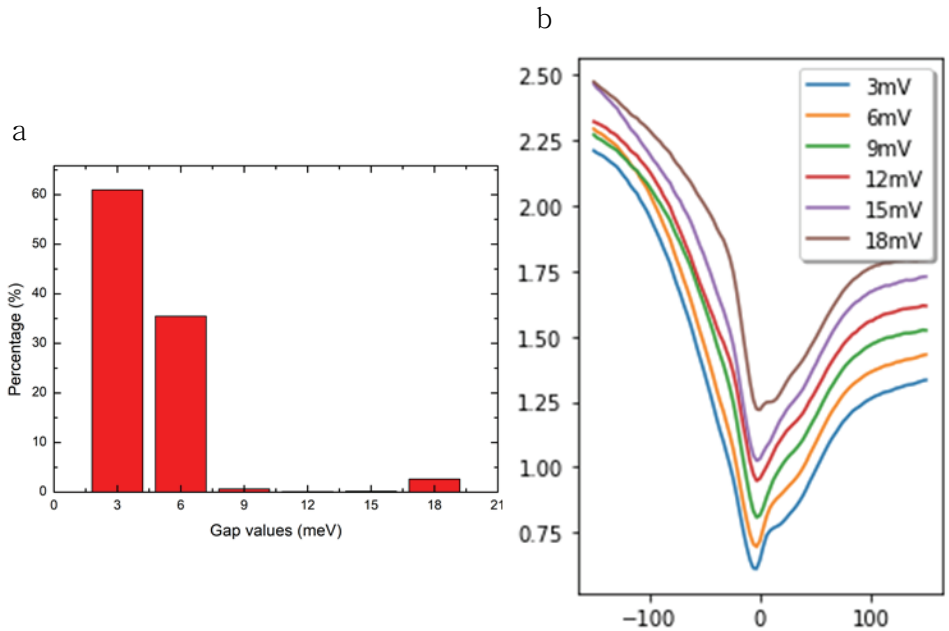

Figure 4.6 Gap histogram and gap sorted conductance spectrum of Ca−1 layer.

(a) Gap histogram of from numerical d2idv2 gap values. Most of the gap values are 3 meV and 6 meV. (b) Averaged of conductance spectrum for each gap values. As bias voltage increase from 3 mV to 15 mV, V−shaped dips in center increase outward. Averaged spectrum of 18mV shows suppression of the dip in center which is different from other gap values averaged spectrum.

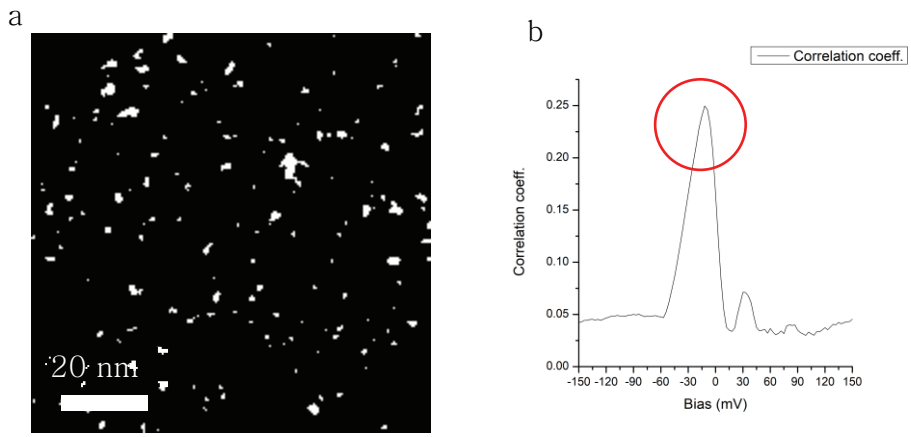

Figure 4.7 Visualization of superconductivity suppressed area and correlation coefficient between that and conductance map..

(a) The visualization of superconductivity suppressed area by using gap values. Gap value with 18 mV area is white color and other area is black. (b) Cross-correlation coefficient between (a) and each bias voltage of conductance map. The peak of cross correlation is at the −12 mV.

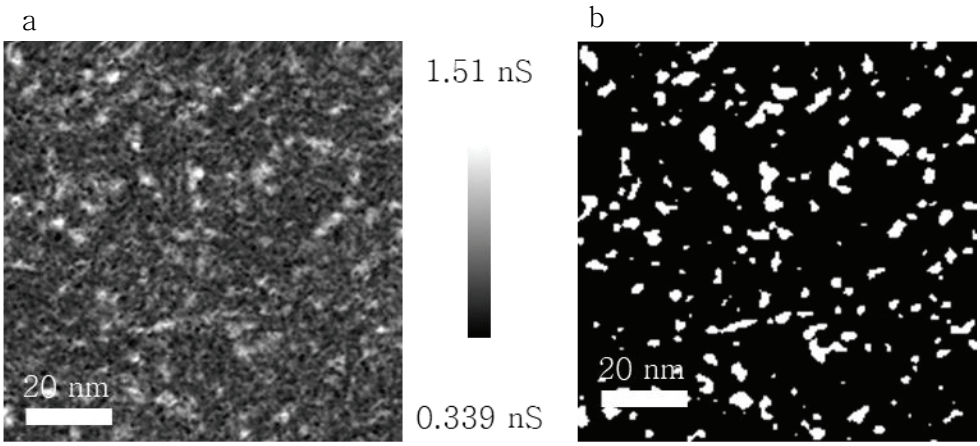

Figure 4.8 Conductance map (bias voltage = −12 mV) and bright spot extracted map.

(a) Conductance map of bias voltage −12 mV which is where cross correlation coefficient is maximized. Conductance map shows bright features. (b) Bright features in (a) is masked as white color and the other area as black color. The percentage of white area is 10.18 %.

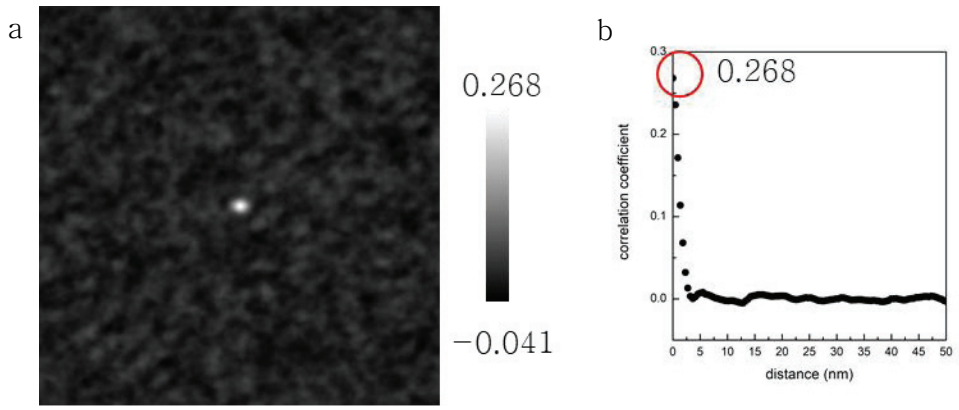

Figure 4.9 Cross correlation and its azimuthal average.

(a) Cross correlation between superconductivity suppressed area (figure 4.7 (a)) and masked image of bright feature in conductance map at bias voltage −12 mV (figure 4.8 (b)). (b) Azimuthal averaged of cross correlation map (a). It shows localized correlation. Peak is at zero distance and cross correlation coefficient is 0.268. Cross correlation coefficient decays as distance is increased and reaches to almost zero after 2 nm.

4.3. La dopants on underlying layer

What is the origin of white features in the conductance map? To investigate what those are, a direct comparison between the conductance map (figure 4.8) and the topographic image (figure 4.2 (a)) was carried out. It is hard to find any similarity between them. After that, I focused on the ratio of those features, which is 10.18 %. That value is close to the La nominal doping ratio (10 %) of this sample.

To verify those features are originated from La dopants, comparison this to the result of the sample in the similar situation was carried out. The hint of the origin of those features was found in the STM experiment on $(Sr_{1-x}La_x)_3Ir_2O_7$ by Wang *et al.* [52]. $(Sr_{1-}$

$_{x}La_{x})_3Ir_2O_7$ has two important similarities to $Ca_{0.9}La_{0.1}FeAs_2$. One is both have La dopants which have 3+ valence. The other is Sr and Ca are in the same Alkaline Earth family with the same valence 2+.

Wang *et al.* showed that La dopants of the top surface (Sr1 layer in figure 4.10(a)) can be seen in the topographic image (figure 4.10 (b)) and La dopants in underlying Sr layer (Sr2 layer in figure 4.10 (a)) were not detected in the topographic image but detected in conductance map (figure 4.10 (c)). Conductance spectra on those two different located La dopants show different behavior. The spectrum taken above the location of La dopants in Sr2 layer shows a sharp peak around −15 mV whereas spectrum La dopants in Sr1 layer has different feature and does not show the peak around −15 mV.

Those are same in $Ca_{0.9}La_{0.1}FeAs_2$. The terminated layer is Ca−1 layer (indicated by the blue line in figure 4.11(a)). White features are detected in the conductance map at the bias voltage −12 mV (figure 4.8). Those features are not detected in the topographic image (figure 4.2(a)) but detected in the conductance map. The average of spectra taken on the white area of figure 4.8 (b) (the red line figure 4.11 (b)) shows peaks around −10 meV whereas the averaged spectrum of the entire field of view (black line in figure 4.11 (b)) does not.

From same results on $(Sr_{1-x}La_x)_3Ir_2O_7$ and the ratio of 10.18 %, which is very close to the nominal doping level 10 %, these white features in conductance map can be concluded as La dopants of underlying Ca−2 layer (indicated by the red line in figure 4.11(a)).

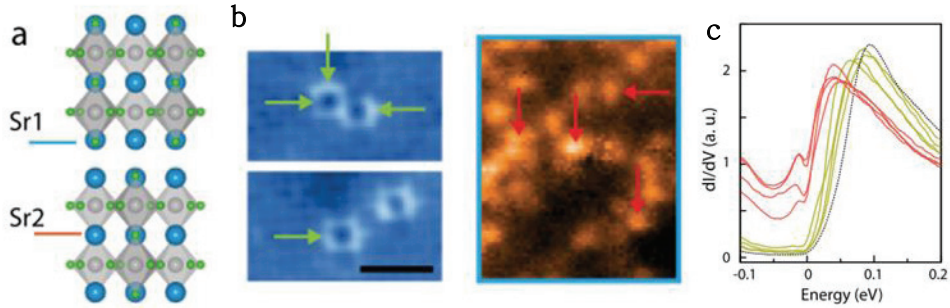

Figure 4.10 STM result on $(Sr_{1-x}La_x)_3Ir_2O_7$

(a) Crystal structure of $(Sr_{1-x}La_x)_3Ir_2O_7$. Sr1 is indicated by blue line which is terminated by sample cleaving. Sr2 is indicated by red line which is not terminating surface. (b) Topographic image which shows La dopants (green arrows) on terminated Sr1 layer. (c) Conductance map of zero bias voltage. The red arrows indicate La dopants on Sr2 layer which is two-layer-below from terminated layer. Those La dopants in Sr2 layer are not located in topographic image. (d) Point spectrum taken on arrows in (b) and (c). Spectra taken on La dopants on Sr2 layer show peak around –15 meV. Reproduce from [52].

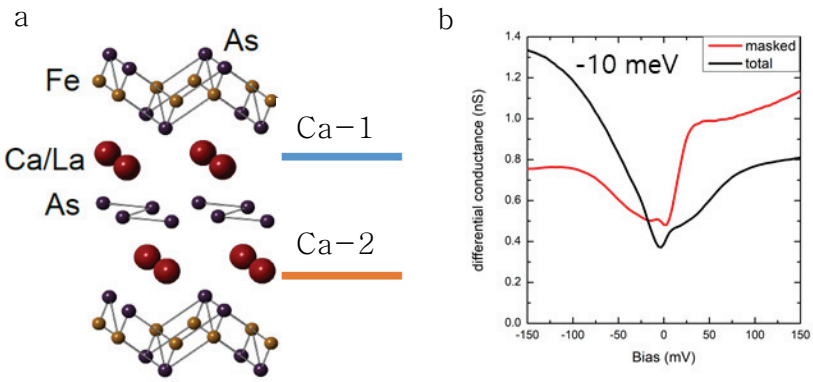

Figure 4.11 Indication of Ca−1 layer and Ca−2 layer on crystal structure of sample and averaged conductance spectra in the entire field of view and white feature area.

(a) Crystal structure of $Ca_{0.9}La_{0.1}FeAs_2$. Blue line indicates the Ca−1 layer (blue) which is terminated layer and red line indicates underlying Ca−2 layer. (b) (Black curve) Average of spectra taken on entire field of view of figure 4.2 (a). (Red curve) Average of spectra taken on white color area of figure 4.8 (b). Red spectrum shows peak at −10 mV bias voltage.

4.4. Summary

In Ca−1 layer, by the numerical d^2I/dV^2 methodology, inhomogeneous gap distribution was shown. From comparison to the STM experiment on $(Sr_{1-x}La_x)_3Ir_2O_7$ and percentage of area, La dopants are located both in energy and real space. The cross-correlation study shows La dopants disturb a superconductivity locally. Someone may think it does not make sense because La dopants seem to be essential to make $Ca_{0.9}La_{0.1}FeAs_2$ as a superconductor. But the same phenomenon was already reported in the case of cuprates superconductor. McElroy *et al.* [53] reported that oxygen dopants in $Bi_2Sr_2CuCa_2O_{8+x}$ make local disturbance on superconductivity.

Chapter 5. Superconductivity through crevices of Ca/La layer above FeAs layer.

As mentioned in chapter 4, the calculation of $CaFe_2As_2$ predicted that Ca layer will show the 2x1 surface reconstruction if Ca layer is terminated in $CaFe_2As_2$. The Ca/La layer above FeAs layer in $Ca_{0.9}La_{0.1}FeAs_2$ (Ca−2 layer) (figure 5.1) is much similar to that situation than Ca−1 layer because Ca−2 layer is right above FeAs layer as in the case of the $CaFe_2As_2$. Therefore, Ca−2 layer also predicted to show 2x1 surface reconstruction.

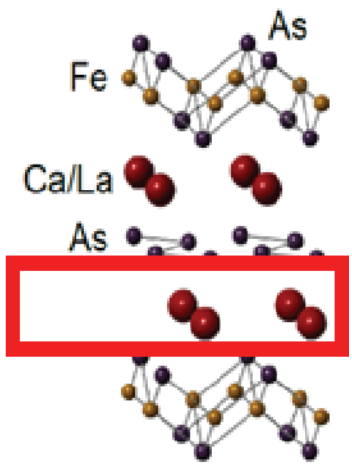

Figure 5.1 Crystal structure and Ca−2 layer.

The crystal structure of $Ca_{0.9}La_{0.1}FeAs_2$. The red box indicates Ca/La layer above FeAs layer (Ca−2 layer) which is discussed in this chapter.

Figure 5.2 is a topographic image taken on Ca−2 layer which size is 80 nm x 40 nm with a condition of −60 mV bias voltage and 60 pA setpoint current. The topographic image again shows the 2x1 surface reconstruction like other surfaces discussed earlier chapters. The major difference between the topographic image compared to Ca−1 layer (figure 4.2 (a)) is Ca−2 layer has a lot of deep crevices in the topographic image.

.

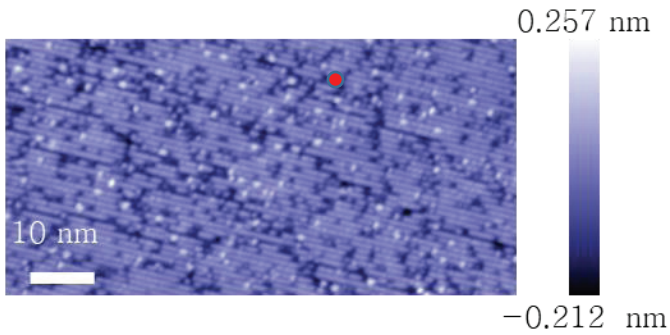

Figure 5.2 Topographic image of Ca−2 layer.

The topographic image (−60 mV / 60 pA) taken on Ca−2 layer. It shows 2x1 surface reconstruction. There are many dark crevices in topographic image and some of them make long 1−D feature.

Figure 5.3 is a point spectrum (black) taken on above one of those crevices. The point spectrum shows a well−defined superconducting gap feature with definite coherence peaks which is much evident than that taken above FeAs layer (black curve in figure 3.2 (b)). Dynes formula [54] was used to fit that spectrum. Dynes formula is

$$\rho(\mathrm{E}, \Gamma) = A \times \mathrm{Re}\left(\frac{E + i\Gamma}{\sqrt{(E + i\Gamma)^2 - \Delta^2}}\right)$$

E is energy, Γ is scattering rate and as it increases, the coherence peak is suppressed. Δ is superconducting gap size.

The red line in figure 5.3 is Dynes formula fitting on point spectrum. The gap value is 9.71 meV and Γ is 3.10 meV. The fitted gap value is similar to that of FeAs layer (12 meV to 14 meV) but slightly smaller.

The conductance map was not obtained fully in the area of figure 5.2 due to a tip change during measurement but remarkable phenomena was observed on that measurement. The topographic image (−60 mV/60 pA, 80 nm x 10 nm) simultaneously taken with the conductance map is in figure 5.4(a) which is the lower part of figure 5.2. Figure 5.4 (b) is the conductance map of zero bias voltage. Evident particle−hole symmetric dip features are observed in the dark area of figure 5.4 (b) and that area is depicted as red color in figure 5.4(a). Figure 5.4(c) is the average of conductance spectra of the entire field of view in figure 5.4(a) (black) and dip exist area (red area in figure 5.4 (a)) (red). Those two averaged spectra show a clear difference. The average of entire spectra (black) shows similar behavior to the averaged spectrum of Ca−1 layer (black curve in figure 4.2 (b)) of low energy without a minimum point shift. The averaged spectrum of evident dip feature area shows a clear particle−hole symmetric spectrum and dip which is similar to figure 5.3 without the superconducting coherence peak. That difference is due to averaging time. The conductance map was set to have 256 x 128 pixel resolution. To measure the conductance map in a reasonable time, the point spectrum should be taken around 4 seconds. But the point spectrum in figure 5.3 was not taken during the measurement of the conductance map so it is possible to choose measurement time freely and that was measured in 120 seconds which is 30 times longer. The shorter measurement time in conductance map makes the point spectrum without the coherence peak. Like the location where the point spectrum in figure 5.3, the red area in the topographic image (figure 5.2) coincides with crevices.

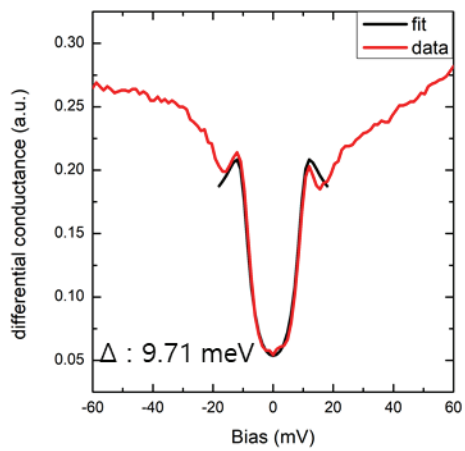

Figure 5.3 Point spectrum taken on crevices.

Point spectrum (red) taken on crevices (red dots in figure 5.2). It shows evident coherence peak and clear particle-hole symmetric behavior. Black line is fitting result by Dynes formula. It matches very well to experiment result and gap value from fitting is 9.71 mV.

What is the reason we can see the superconducting gap feature in the spectrum taken on crevices and that spectrum shows much more a particle-hole symmetric property than that of FeAs layer (figure 3.2 (b))?

As already discussed in chapter 3, the topographic image taken on FeAs layer (figure 3.2 (a) and figure 3.3) shows 2x1 the surface reconstruction. Also, FeAs layer is negatively charged. Those two components of FeAs terminated layer disturbs the spectrum on FeAs layer and make it particle-hole asymmetric. Now let's think about the Ca-2 layer which is right above the FeAs layer. First, we can think of the doping effect from Ca-2 layer. Second is the charge-neutral surface which will not hamper the spectrum taken on Ca-2 layer. Last is the surface reconstruction. Due to Ca-2 layer is terminated surface, the underlying FeAs layer does not need to have the 2x1 surface reconstruction. Therefore, if the measurement is taken above crevices on Ca-2 layer, it can be regarded as a direct measurement on FeAs layer without the 2x1 surface reconstruction and the surface charge effect. Those are why the spectrum on crevices of Ca-2 layer shows much particle-hole symmetric than FeAs layer and this layer can be concluded as Ca-2 layer.

In this section, Ca-2 layer is identified by the topographic image and spectra above crevices which make the direct measurement on FeAs layer without the 2x1 surface reconstruction possible.

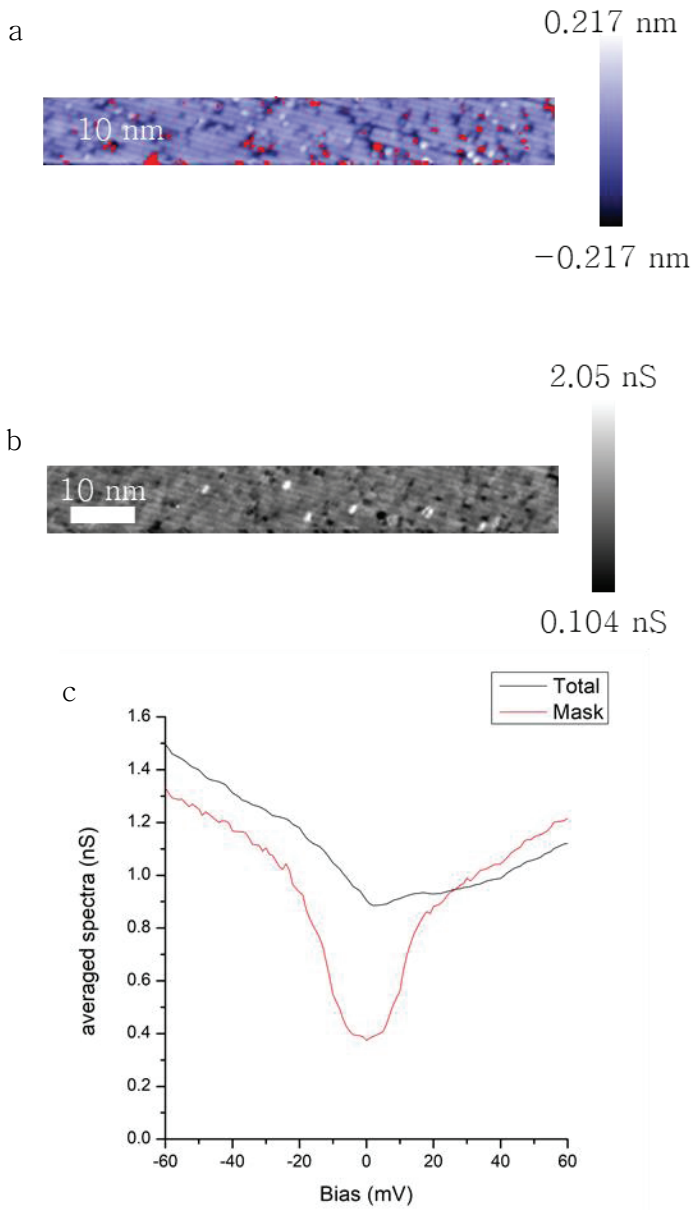

Figure 5.4 Topographic image and conductance map taken at Ca−2 layer and averaged spectra.

(a) Topographic image taken simultaneously with conductance map. Target area was figure 5.2. Due to tip change during experiment, size is smaller. (b) Conductance map of zero bias simultaneously with (a). (c) Averaged spectrum of entire field of view of (a) (black) and averaged spectrum of red area in (a) (red). Total averaged spectrum shows particle hole asymmetric behavior whereas averaged spectrum of red area shows clear particle−hole symmetric behavior.

Chapter 6. Dirac cone dispersion and zero bias conductance peak on As chain layer

As zigzag chain layer (figure 6.1) is a unique feature of $Ca_{1-x}RE_xFeAs_2$ [36–38,55] type of Fe-based superconductor. The existence of this unique layer induces interesting properties in $Ca_{0.9}La_{0.1}FeAs_2$.

First is electron pockets around X points of Fermi surface, which is not in other types of Fe-based superconductors. Theoretical calculation predicted those electron pockets have the anisotropic Dirac cone feature [45] and the ARPES experiment measured those anisotropic Dirac cone dispersion experimentally [56].

Second is As zigzag chain layer is a possible topological insulator and due to that, $Ca_{0.9}La_{0.1}FeAs_2$ is one possible candidate that can host a topological superconductivity [45].

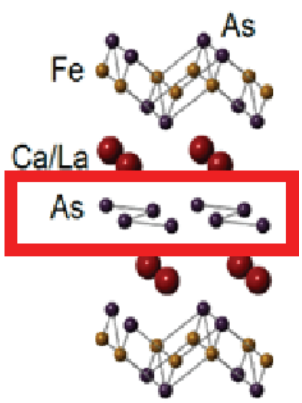

Figure 6.1 Crystal structure and As zigzag chain layer.

The crystal structure of $Ca_{0.9}La_{0.1}FeAs_2$. The red box indicates As zigzag chain layer which is discussed in this chapter. As zigzag chain layer is above Ca-2 layer.

6.1. Identification of As zigzag chain layer.

The topographic image is in figure 6.2 (a), which is a size of 63 nm x 63 nm with the bias voltage of −200 mV and the setpoint current 200 pA. Figure 5.3 is a zoomed−in topographic image of figure 6.2 (a) to show the 2x1 surface reconstruction more clearly. An average of conductance spectra taken above the entire field of view of figure 6.2 (a) is in figure 6.2 (b). It shows a very broad V−shape spectrum compared to the aforementioned three layers' averaged conductance spectrum (black curves in figure 3.2 (b), figure 4.2 (b), and figure 5.4 (c)) and different behavior. The averaged spectrum on this layer shows that this layer is a completely different layer from the other 3 discussed layers so this layer is concluded as only remaining possible As zigzag chain layer.

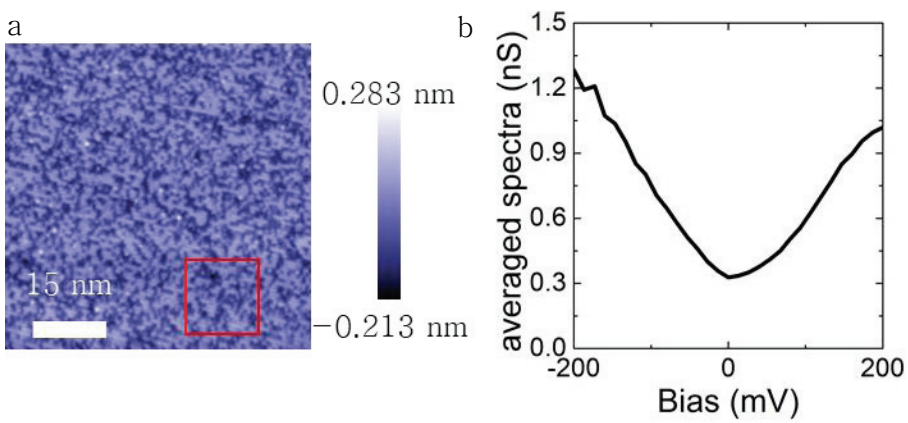

Figure 6.2 Topographic image and averaged conductance spectrum.

(a) Topographic image (−200 mV/200 pA) taken above As zigzag chain layer size of 63 nm x 63 nm. (b) Average of spectra taken entire field of view of (a). It shows very broad V−shaped feature.

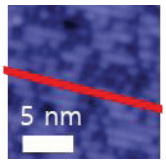

Figure 6.3 Zoomed in topographic image.

Zoomed in topographic image of red box in figure 6.2 (a). 2x1 surface reconstruction can be seen clearly. Red line indicates the direction of 2x1 surface reconstruction.

6.2. Observation of Dirac cone like dispersion.

Figure 6.4 are conductance maps of As chain layer bias voltage from −200 mV to −93.3 mV. There are some 1D features along the direction of the yellow line in fig 6.4. To investigate the property of conductance maps on As zigzag chain layer, Fourier transform was applied on conductance maps. Figure 6.5 (a) is the Fourier transform of the conductance map of the bias voltage −200 mV in figure 6.4. Line profiles were taken along the yellow line in figure 6.5 (a) which is the same direction of the 1D feature in conductance maps (figure 6.4). Due to the peaks on 90 degrees of the yellow line are too strong, it is hard to visualize the dispersion of peaks along the yellow line. To visualize, normalized line profiles are plotted in figure 6.5 (b). The largest peak in each line profile shows a decrease at first and increase after a certain bias voltage as applied bias voltage increases (green line in figure 6.5 (b)). The quantitative analysis of those peaks movement with bias voltage change is plotted in figure 6.6. It shows a Dirac cone like dispersion and its center point is at the bias voltage of −146 mV.

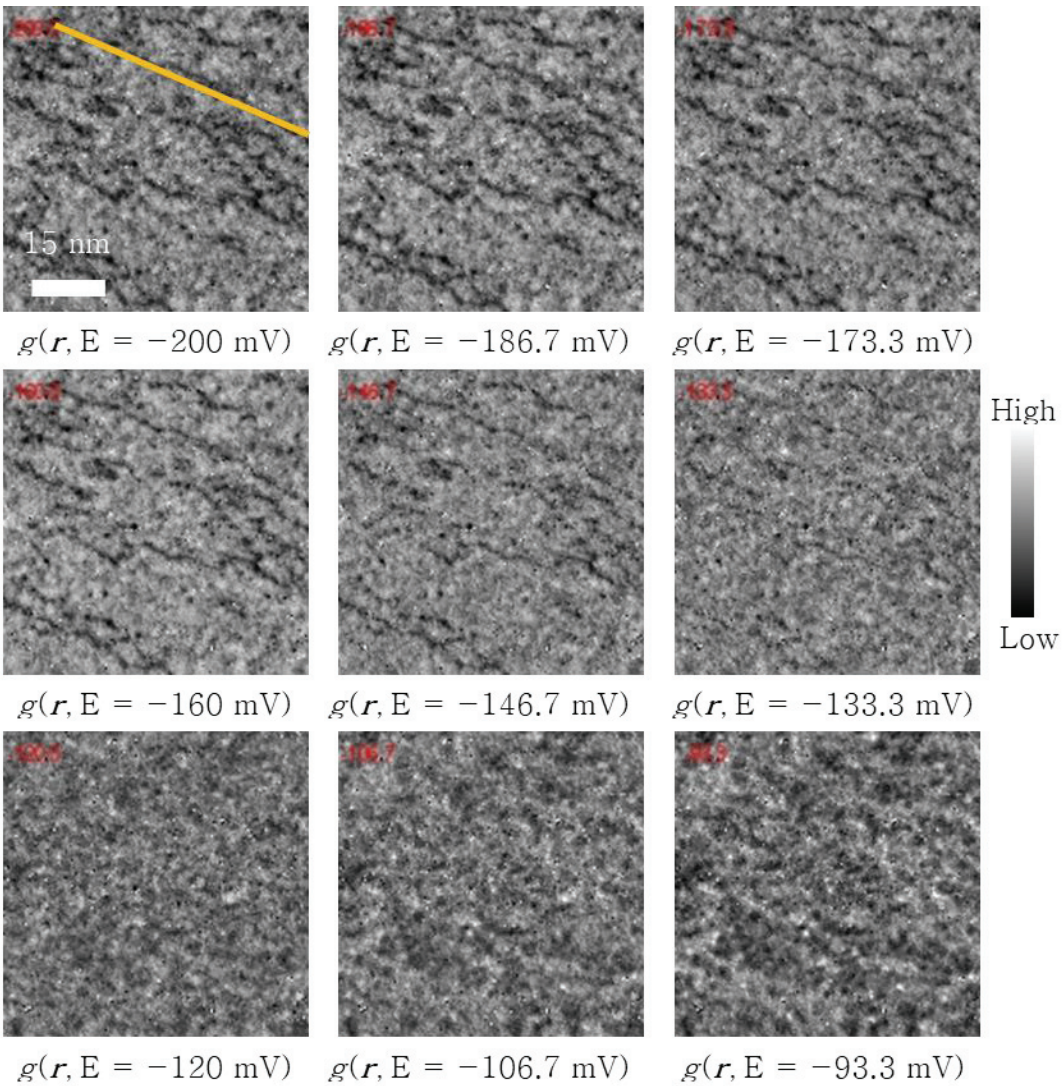

Figure 6.4 Conductance maps on As zigzag chain layer.

Conductance maps which are taken simultaneously with topographic image (figure 6.2 (a)) bias voltage from −200 mV to −93.3 mV with equal difference. There are some 1D features in conductance maps and yellow lines is along those features' direction.

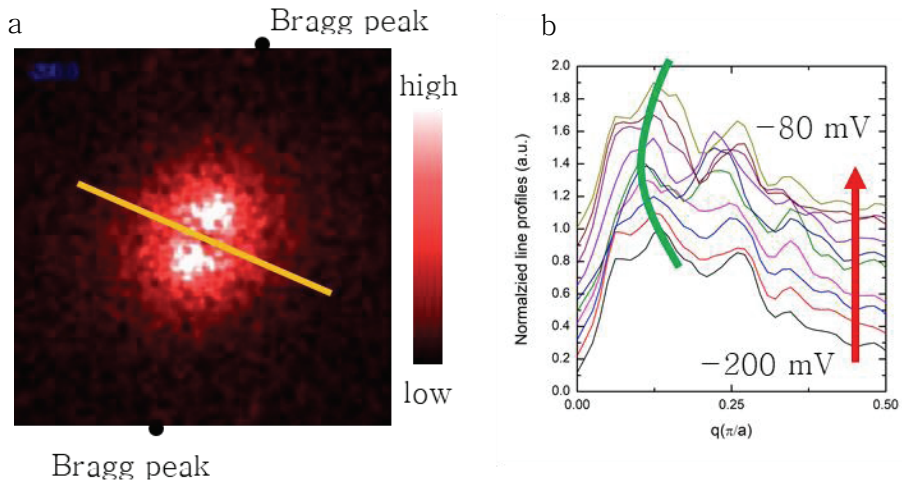

Figure 6.5 Fourier transform of conductance map and Line profiles.

(a) Fourier transform of conductance map of bias voltage −200 mV. Yellow line is line profile direction which is same as that of in figure 6.4. (b) Line profiles of Fourier transform image bias voltage from −200 mV to −80 mV. Green line is to help identification of peaks' movement with bias voltage. It decrease at first but after certain bias voltage, it increases.

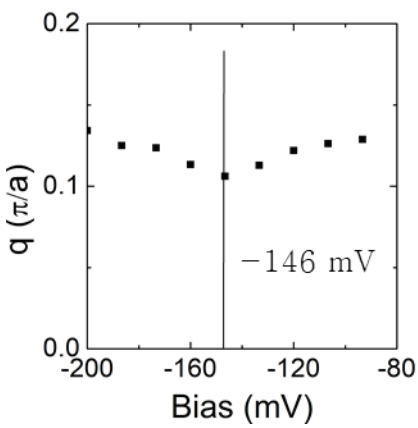

Figure 6.6 Peaks location vs bias voltage.

Location of peaks (indicated by green line in figure 6.5 (b)) vs bias voltage is plotted. It shows Dirac cone like dispersion.

What is the origin of that Dirac cone dispersion? To investigate the origin, the Fermi surface was used. Figure 6.7 (a) is calculated Fermi surface [56]. The line of connection between two Bragg peaks in the Fourier transform image (black dots in figure 6.5 (a)) coincide the line between X point of Fermi surface. From that information, direction of line profiles and size of peak's location in line profiles, only possible bands are electron pockets around X (red circles in green dashed circle in figure 6.7 (a)). As mentioned earlier, those pockets are the unique property of $Ca_{0.9}La_{0.1}FeAs_2$ because they are originated from As zigzag chain layer. The STM result was matched to ARPES measurement on that electron pocket [56] in figure 6.7 (b). Green dots in the green circle are from figure 6.6 with the conversion from q to k vector. The STM result and the ARPES measurement match very well with −56 meV energy shift. That is similar to the energy difference between the STM result and the ARPES result on FeAs layer (figure 3.9 (b)) in chapter 3. As discussed earlier in chapter 3, this energy shift in the experiment above As zigzag chain layer can be explained by the difference between the nominal doping

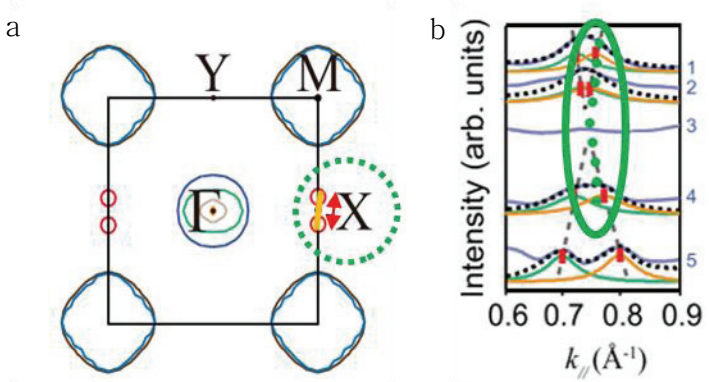

Figure 6.7 Calculated Fermi surface and Fit STM result in ARPES measurement.

(a) Calculated Fermi surface of $Ca_{0.9}La_{0.1}FeAs_2$. The only possible band that can make peaks in figure 6.5(b) both size and angle is red pocket around X point of Fermi surface (inside of green dotted circle). (b) STM result (green dots inside of green circle) is fitted to ARPES measurement. Reproduced from [46], with the permission of AIP publishing.

level and the actual doping level of $Ca_{0.9}La_{0.1}FeAs_2$.

6.3. Observation of zero bias conductance peaks.

What is the origin of the 1D feature in conductance maps on As zigzag chain layer (figure 6.4)? The clue to this question was found on the Ca−2 layer. Figure 6.8 (a) is a topographic image of As zigzag chain layer which is simultaneously taken with conductance maps (figure 6.4 and figure 6.8 (c)). Figure 6.8 (b) is an enlarged topographic image and the 2x1 surface reconstruction direction is indicated by the red line. That red line and 1D feature line (the yellow line in figure 6.8 (c)) shows the direction of those two lines are different. Figure 6.8 (d) is a topographic image take above Ca−2 layer and the red line and the yellow line have the same direction as those in figure 6.8 (a), (b), and (c). As you can see in figure 6.8 (d), the red line coincides with the 2x1 surface reconstruction line of Ca−2 layer and the yellow line coincide with the 1D like crevice on Ca−2 layer. From those coincidences, the 1D feature in conductance maps taken above As chain layer is originated from 1D like crevices of underlying Ca−2 layer.

I will briefly explain this situation again with schematic diagrams of each related layers. There is a FeAs layer (figure 6.9) which is the essential layer for superconductivity.

Ca−2 layer is right above FeAs layer (figure 6.10). As already mentioned in chapter 5, crevices exist in Ca−2 layer and particle−hole symmetric superconducting spectra without the 2x1 surface reconstruction on FeAs layer is measured on that crevice area(figure 6.10 (b)).

From different conductance spectrum behavior above Ca−2 layer (figure 6.10 (a)) and crevices of Ca−2 layer (figure 6.10 (b)), it is a reasonable prediction that there might be different conductance spectrum behavior between As chain layer above normal Ca−2 layer

and crevices of Ca−2 layer. Remarkably, there is a difference between the conductance spectrum on those two different areas and spectrum taken above As chain layer above crevices of Ca−2 layer shows a zero bias conductance peak (figure 6.11 (b)) whereas conductance spectrum on other area shows broad V−shaped behavior (figure 6.11 (a)).

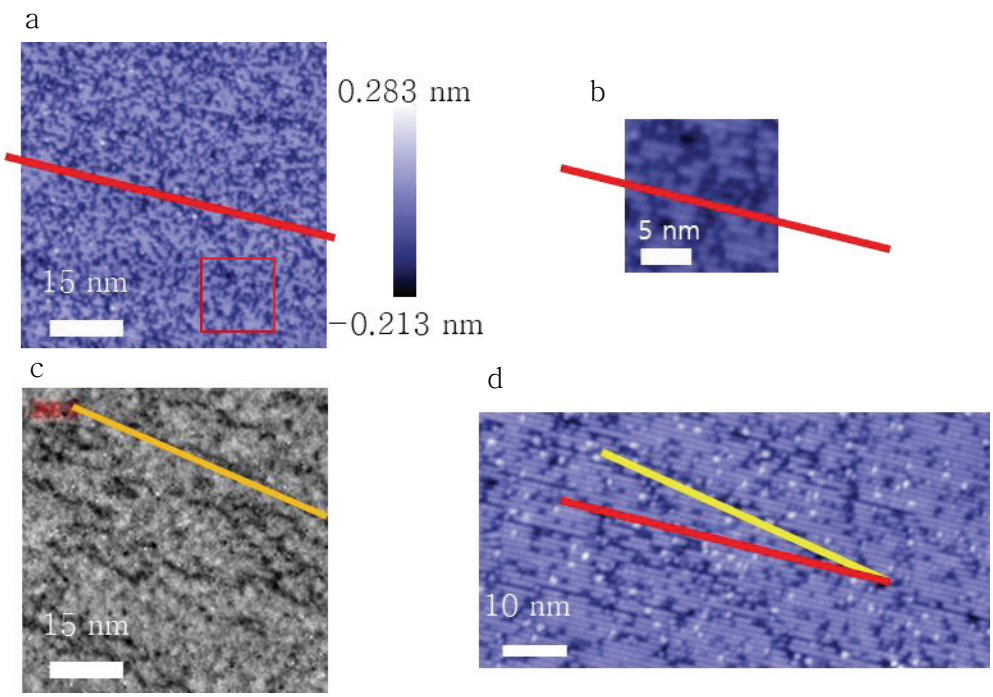

Figure 6.8 Topographic image and conductance map on As zigzag chain layer and topographic image on Ca−2 layer.

(a) Topographic image in figure 6.2 (a). Red line is for indication of 2x1 surface reconstruction. (b) Zoom in of red box in (a) (same as in figure 6.3). Red line is for indication of 2x1 surface reconstruction direction. (c) Conductance map at bias voltage of −200 mV on As zigzag chain layer (same as in first image of figure 6.4). Yellow lines in for indication of 1D feature in conductance map. (d) Topographic image of Ca−2 layer (same in figure 5.2). Red line and yellow line are same as in (a), (b) and (c). (d) shows that direction of 2x1 surface reconstruction in As zigzag chain layer. Also, 1D feature in conductance map (c) coincide with crevices on Ca−2 layer.

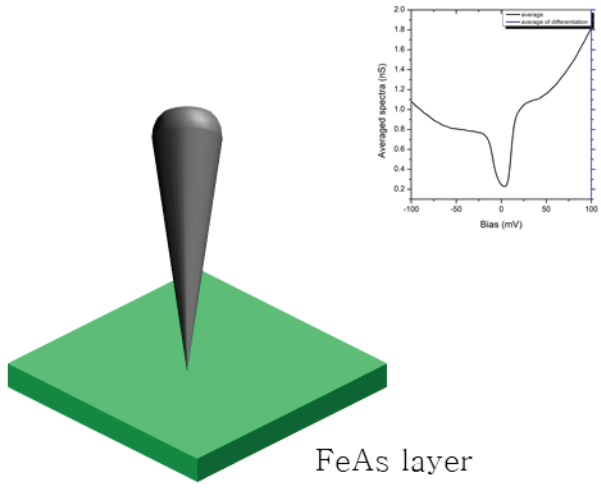

Figure 6.9 The illustration to explain of measurement on As zigzag chain layer 1.

Measurement on FeAs layer. Spectrum shows gap feature all around surfaces.

Figure 6.12 (a) is one example of a point spectrum which shows zero bias conductance peak. Figure 6.12 (b) is the conductance map of As chain layer at the bias voltage −200 mV with an indication of where zero bias conductance peaks exist (red area). The zero bias conductance peak existing point matches well with the 1D feature of the conductance map which is originated from crevices of the underlying Ca−2 layer.

Figure 6.13 (a) is the average of conductance spectrum of the entire field of view of figure 6.12 (a) (black) and only zero bias conductance peak existing area (red). Figure 6.13 (b) is the distribution of zero bias conductance peaks' height. Due to bias voltage resolution is not fine, to study further, more fine resolution of the bias voltage is needed.

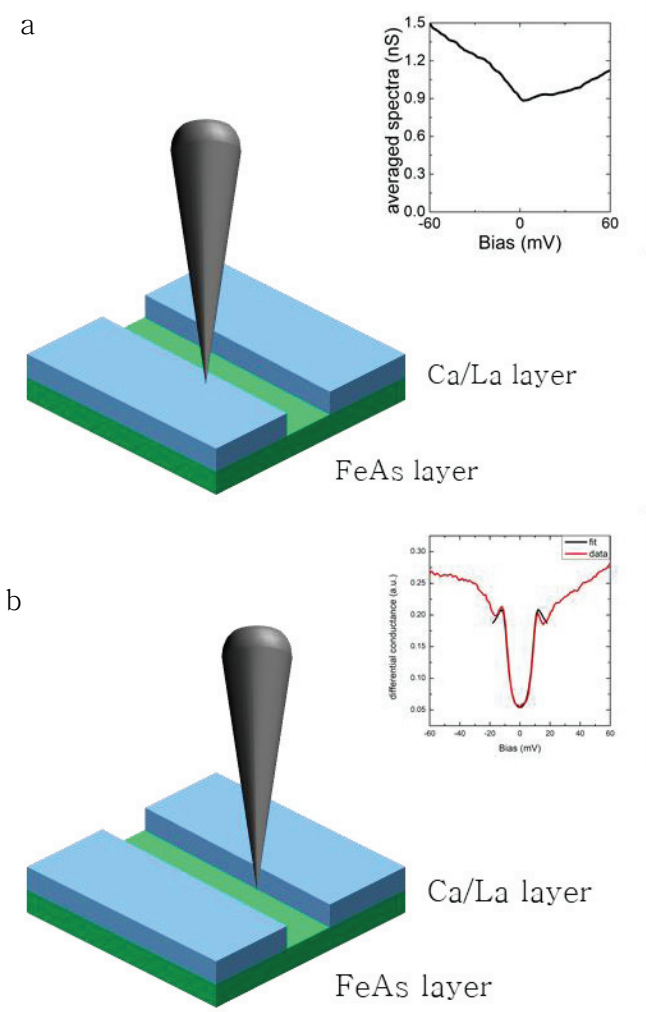

Figure 6.10 The illustration to explain of measurement on As zigzag chain layer 2.

Measurement on Ca-2 layer which is right above FeAs layer. Spectrum above (a) Ca-2 layer and (b) crevices on Ca-2 layer shows clearly different feature. Spectrum above Ca-2 layer shows particle-hole symmetric evident coherence peak superconducting feature.

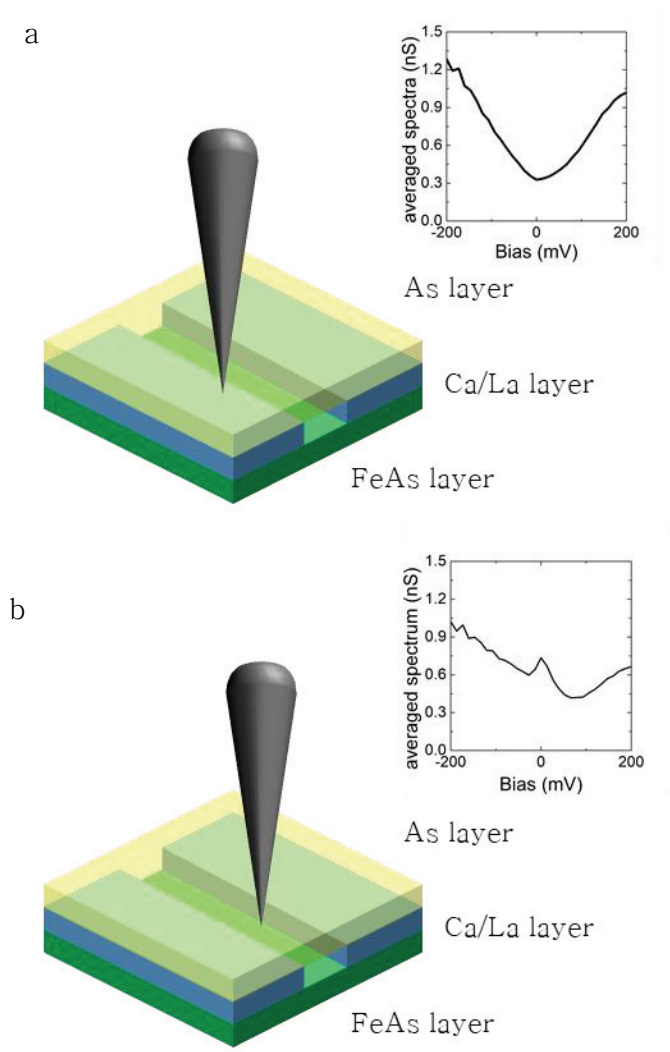

Figure 6.11 The illustration to explain of measurement on As zigzag chain layer 3.

Measurement on As zigzag chain layer which is above Ca-2 layer. Like in the case of Ca-2 layer, existence of crevices on Ca-2 layer makes huge difference in spectrum. (a) Spectrum taken on As zigzag chain layer above Ca-2 layer case shows broad V like spectrum. (b) Spectrum take on As zigzag chain layer above crevices in Ca-2 layer case shows the zero bias conductance peak in some cases.

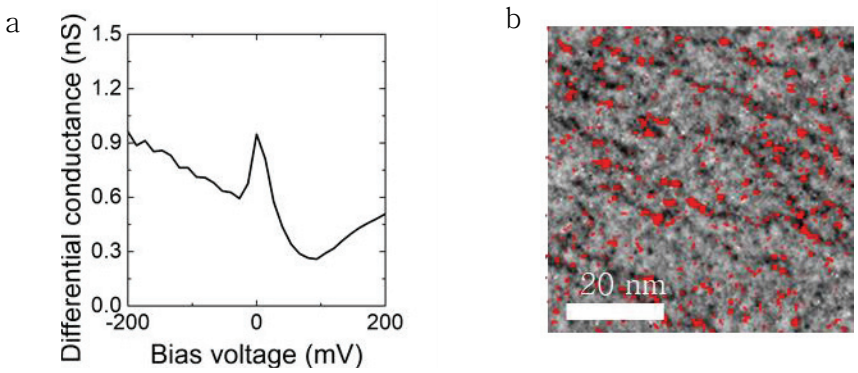

Figure 6.12 Point spectrum and conductance map with zero bias conductance peak area masked.

(a) Point spectrum which shows zero bias conductance peak. (b) Conductance map of −200 mV bias voltage. Red area is where zero bias conductance peak s exist. Those area matches well to dark area which are crevices of Ca−2 layer

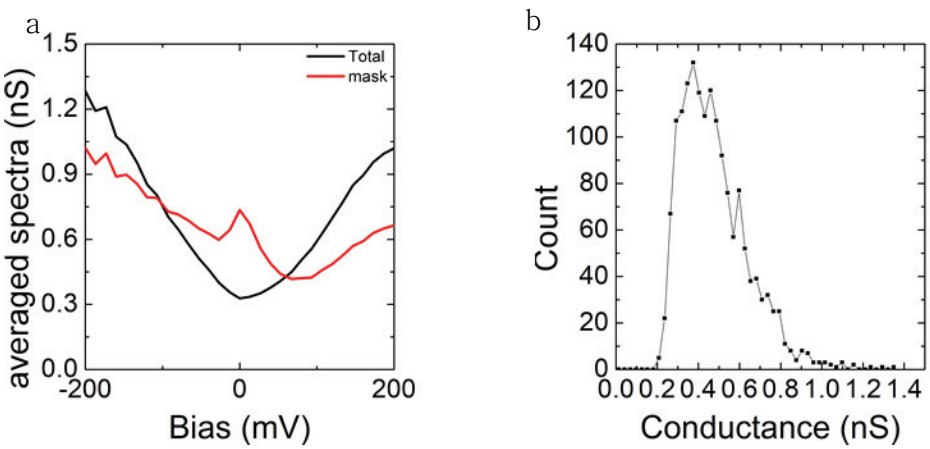

Figure 6.13 Averaged spectrum taken on As zigzag chain layer and distribution of height of the zero bias conductance peaks.

(a) (Black) Average of spectra taken on entire field of view of figure 6.12 (b). (Red) Average of spectra taken on red area of figure 6.12 (b). (b) Distribution of height of the zero bias conductance peaks in figure 6.12 (b).

What is the origin of those zero bias conductance peaks measured only above As zigzag chain layer above crevices of underlying Ca−2 layer? There are several possible origins of zero bias conductance peak.

The first possibility is the Josephson effect [57]. To achieve the Josephson effect in the STM, a superconducting tip is required. The experiment described here was performed by a bear tungsten tip. Still, there is a possibility that the flake of $Ca_{0.9}La_{0.1}FeAs_2$ sample was stuck to the tungsten tip. In that case, the spectrum should show a well−defined superconducting gap feature but it is not in this case (figure 6.13 (a)). The junction resistance of this STM experiment on As zigzag chain layer was 1 GΩ which is very huge compared to the Josephson effect experiments on $Bi_2Sr_2CuCa_2O_{8+x}$ performed by the STM (~300 kΩ at 4.2 K [58] and ~ 100 MΩ at 50 mK [59]). From reasons above, the Josephson effect is not the origin of the observed zero bias conductance peak on As zigzag chain layer.

The second possibility is the Andreev reflection [60]. To achieve the Andreev reflection, a direct superconductor metal junction is needed therefore it is not the case because the STM experiment is vacuum tunneling experiment.

The third possibility is the Andreev bound state [61]. This case also needs the superconducting tip so due to the same reason discussed in the case of the Josephson effect, this possibility can be erased.

The fourth possibility is the Kondo effect which is due to a local magnetic defect [62,63]. From chemical formula, there is no local magnetic impurity in As zigzag chain layer. If those zero bias conductance peaks are affected by Fe atoms in this material then zero bias conductance peak should be observed on the entire field of view of figure 6.12 (b). But as described earlier in this chapter, zero bias conductance peaks were observed locally only above crevices of Ca−

2 layer. From the above reasons, it is possible to eliminate the Kondo effect.

The last possibility in my knowledge is the superconducting proximity effect on topological insulator. Zero bias conductance peaks were detected only on As chain layer above crevices of Ca−2 layer. In chapter 5 (experiment above Ca−2 layer), undisturbed superconducting gap features are observed in the spectrum only above crevices on Ca−2 layer was shown. As zigzag chain layer has a possibility of the topological insulator by theoretical calculation [45]. From those possibilities, this scenario cannot be ruled out.

Ingredients for MZM	Semiconducting nanowire(InSb) On s wave superconductor(NbTiN)	Vortex cores of $FeTe_{0.55}Se_{0.45}$ superconductor(STM)	hexagonal Bi island on superconducting Nb with Fe cluster(STM)	As chain layer on $Ca_{0.9}La_{0.1}FeAs_2$(STM)
Superconductivity	S wave Δ=250μV	**Iron Based Superconductor** Δ=1.8 mV	S wave Δ= 1.5 mV	Iron Based Superconductor Δ= 10 mV
Topologically nontrivial	**1D wire**	$FeTe_{0.55}Se_{0.45}$ surface state	Bi edge state	As chain layer
Spin Orbit Coupling	InSb	Fe, Te	Bi	Fe, La?
Time Reversal Symmetry	In plane B	B field	**Fe clusters**	Fe atoms (AFM but 1D FM in certain direction)

Table 6.1 Comparison to other experiment of zero bias conductance peaks due to topological origin.

Table 6.1 is a comparison to the other three experiments [64–66] on zero bias conductance peak due to topological effect. There are three similarities in my experiment. First is this sample is iron based superconductor like the experiment by Wang *et al.* [66]. Second is it has a 1D feature in Ca−2 layer due to crevices which is similar to 1D wire in the experiment by Mourik *et al.* [64]. The third is it has a ferromagnetic Fe direction due to its antiferromagnetic property which is similar to Fe cluster on the experiment by Jäck *et al.* [65].

If the observed zero bias conductance peak is indeed due to topological effect, it has some uniqueness compared to other experiments. First, it has a relatively larger superconducting gap (~10 meV) and higher critical temperature (~40K). The Fe atom cluster is naturally incorporated and naturally made 1D structure exist. A statistical analysis (for example, like the distribution of zero bias conductance peaks' height illustrated in figure 6.13 (b)) is possible due to the number of zero bias conductance peaks are many compared to other experiments.

To verify it is indeed due to the topological effect, several experiments have to be performed. The temperature dependence experiment (especially above critical temperature) is also needed to verify that zero bias conductance peak is due to superconductivity. Mapping around crevices with high spatial and energy resolution and application of the magnetic field will help to identify this zero bias conductance peak.

The most begging question on $Ca_{0.9}La_{0.1}FeAs_2$ is if As zigzag chain layer introduces a topologically non-trivial states or not. Our observation of the zero bias conductance peak on this material might provide a clue to this answer. We could not come up with any other possible origin for the zero bias conductance peak than a proximity coupling between the superconducting order parameter on Fe/As layer and topologically non-trivial As chain layer as of now. A further theoretical modeling is necessary to draw a definite conclusion.

6.4 Summary

Dirac-cone like dispersion on As zigzag chain layer was observed which is a unique property of this sample compared to other types of iron based superconductors. The dispersion coincides with

ARPES measurement.

From the comparison between conductance map on As zigzag chain layer, the topographic image on As zigzag chain layer and topographic image on Ca-2 layer, the origin of 1D feature in conductance map on As zigzag chain layer is nothing but due to crevices of underlying Ca-2 layer.

Zero bias conductance peak on As zigzag chain layer above crevices of Ca-2 layer is found which might be possibly due to superconductivity effect on topological insulator suggesting this sample might be a new playground to find a zero bias conductance peak due to topological effect and provide a clue where to look to verify an existence of topological superconductivity on this material.

Chapter 7. Conclusion

Motivated by a prediction that $Ca_{0.9}La_{0.1}FeAs_2$ might be a topological superconductor, we performed a thorough atomic-scale spectroscopic imaging study on this relatively new superconducting compound. As a result, all four possible terminating layers were successfully characterized via a topography, conductance mapping as well as its Fourier transform analysis. We discovered an unusual zero bias conductance peak on As zigzag chain layer which might provide a clue to the verification of the existence of non-trivial topology in this material.

In chapter 1, a detailed description of the low-temperature SI-STM system was presented including a design philosophy, essential components as well as the ULV laboratory. In chapter 2, a brief background of Ca0.9La0.1FeAs2 was introduced.

In chapter 3, a spectroscopic property of the FeAs layer is discussed. This layer is identified by surface reconstruction of the topographic image, shift of spectrum by charged surface, and homogeneous gap distribution. The distribution of the gap is visualized by the numerical d^2I/dV^2 method. A nematic feature was observed from the conductance map. Using a Fourier transform analysis, the origin of nematic feature is found to be hole-like band near zone center which has d_{xz} and d_{yz} orbital character.

In chapter 4, characterization of a Ca/La layer above As zigzag chain layer was discussed is described. Ca/La terminating surface is identified by topographic images and a shift of the conductance spectra. This layer exhibits an inhomogeneous gap distribution. By using the gap map by d^2I/dV^2 methodology, gap sorted spectrum, and conductance map, La dopants are located in energy and real space. Local superconductivity suppression by La dopants is discovered by

a cross-correlation study.

In chapter 5, Ca/La layer above FeAs layer is discussed. Through crevices on the layer, a clear superconducting gap was probed suggesting that the FeAs layer can be directly accessed without a suppression of superconductivity unlike on a bare FeAs layer.

In chapter 6, I discussed the data of As zigzag chain layer. The Dirac cone dispersion which is the unique property due to As zigzag chain layer is observed by using Fourier transform analysis. Numerous zero bias conductance peaks were observed on areas where crevices of underlying Ca/La layer above FeAs layer were visible. The discovery of zero bias conductance peaks on As zigzag chain layer is an intriguing one begging for a further theoretical explanation. Whether such zero bias conductance peaks are topologically non trivial is not clear as of this thesis written, but at least now we know where to look for a clue. Also, I hope my study provides a guideline for further research topics on Fe-based 112 superconductor.

Bibliography

[1] G. Binnig, H. Rohrer, C. Gerber, and E. Weibel, Phys. Rev. Lett. **49**, 57 (1982).

[2] C. J. Chen, *Introduction to Scanning Tunneling Microscopy* (Oxford University Press, 2007).

[3] J.-J. Kim, S. H. Joo, K. S. Lee, J. H. Yoo, M. S. Park, J. S. Kwak, and J. Lee, Rev. Sci. Instrum. **88**, 043702 (2017).

[4] S. H. Pan, E. W. Hudson, and J. C. Davis, Rev. Sci. Instrum. **70**, 1459 (1999).

[5] H. K. Onnes, Commun. Phys. Lab. Univ. Leiden **12**, 120 (1911).

[6] W. Meissner and R. Ochsenfeld, Naturwissenschaften **21**, 787 (1933).

[7] Proc. R. Soc. London. Ser. A - Math. Phys. Sci. **149**, 71 (1935).

[8] V. L. Ginzburg, L. D. Landau, M. A. Leontovich, and V. A. Fok, JETP **20**, 1064 (1950).

[9] J. Bardeen, L. N. Cooper, and J. R. Schrieffer, Phys. Rev. **106**, 162 (1957).

[10] J. G. Bednorz and K. A. Müller, Zeitschrift Für Phys. B Condens. Matter **64**, 189 (1986).

[11] M. K. Wu, J. R. Ashburn, C. J. Torng, P. H. Hor, R. L. Meng, L. Gao, Z. J. Huang, Y. Q. Wang, and C. W. Chu, Phys. Rev. Lett. **58**, 908 (1987).

[12] H. Maeda, Y. Tanaka, M. Fukutomi, and T. Asano, Jpn. J. Appl. Phys. **27**, L209 (1988).

[13] A. Schilling, M. Cantoni, J. D. Guo, and H. R. Ott, Nature **363**, 56 (1993).

[14] Y. Kamihara, H. Hiramatsu, M. Hirano, R. Kawamura, H. Yanagi, T. Kamiya, and H. Hosono, J. Am. Chem. Soc. **128**, 10012 (2006).

[15] J.-F. Ge, Z.-L. Liu, C. Liu, C.-L. Gao, D. Qian, Q.-K. Xue, Y. Liu, and J.-F. Jia, Nat. Mater. **14**, 285 (2015).

[16] A. P. Drozdov, M. I. Eremets, I. A. Troyan, V. Ksenofontov, and S. I. Shylin, Nature **525**, 73 (2015).

[17] A. P. Drozdov, P. P. Kong, V. S. Minkov, S. P. Besedin, M. A. Kuzovnikov, S. Mozaffari, L. Balicas, F. F. Balakirev, D. E. Graf, V. B. Prakapenka, E. Greenberg, D. A. Knyazev, M. Tkacz, and M. I. Eremets, Nature **569**, 528 (2019).

[18] Y. Kamihara, T. Watanabe, M. Hirano, and H. Hosono, J. Am. Chem. Soc. **130**, 3296 (2008).

[19] F.-C. Hsu, J.-Y. Luo, K.-W. Yeh, T.-K. Chen, T.-W. Huang,

P. M. Wu, Y.-C. Lee, Y.-L. Huang, Y.-Y. Chu, D.-C. Yan, and M.-K. Wu, Proc. Natl. Acad. Sci. **105**, 14262 (2008).
[20] Y. Han, W. Y. Li, L. X. Cao, X. Y. Wang, B. Xu, B. R. Zhao, Y. Q. Guo, and J. L. Yang, Phys. Rev. Lett. **104**, 017003 (2010).
[21] X. Lai, H. Zhang, Y. Wang, X. Wang, X. Zhang, J. Lin, and F. Huang, J. Am. Chem. Soc. **137**, 10148 (2015).
[22] X. C. Wang, Q. Q. Liu, Y. X. Lv, W. B. Gao, L. X. Yang, R. C. Yu, F. Y. Li, and C. Q. Jin, Solid State Commun. **148**, 538 (2008).
[23] D. R. Parker, M. J. Pitcher, P. J. Baker, I. Franke, T. Lancaster, S. J. Blundell, and S. J. Clarke, Chem. Commun. 2189 (2009).
[24] Z. Deng, X. C. Wang, Q. Q. Liu, S. J. Zhang, Y. X. Lv, J. L. Zhu, R. C. Yu, and C. Q. Jin, EPL (Europhysics Lett. **87**, 37004 (2009).
[25] M. Rotter, M. Tegel, and D. Johrendt, Phys. Rev. Lett. **101**, 107006 (2008).
[26] P. M. Shirage, K. Miyazawa, H. Kito, H. Eisaki, and A. Iyo, Appl. Phys. Express **1**, 081702 (2008).
[27] K. Sasmal, B. Lv, B. Lorenz, A. M. Guloy, F. Chen, Y.-Y. Xue, and C.-W. Chu, Phys. Rev. Lett. **101**, 107007 (2008).
[28] X. H. Chen, T. Wu, G. Wu, R. H. Liu, H. Chen, and D. F. Fang, Nature **453**, 761 (2008).
[29] G. F. Chen, Z. Li, D. Wu, G. Li, W. Z. Hu, J. Dong, P. Zheng, J. L. Luo, and N. L. Wang, Phys. Rev. Lett. **100**, 247002 (2008).
[30] Z. A. Ren, J. Yang, W. Lu, W. Yi, G. C. Che, X. L. Dong, L. L. Sun, and Z. X. Zhao, Mater. Res. Innov. **12**, 105 (2008).
[31] Z.-A. Ren, J. Yang, W. Lu, W. Yi, X.-L. Shen, Z.-C. Li, G.-C. Che, X.-L. Dong, L.-L. Sun, F. Zhou, and Z.-X. Zhao, EPL (Europhysics Lett. **82**, 57002 (2008).
[32] J.-W. G. Bos, G. B. S. Penny, J. A. Rodgers, D. A. Sokolov, A. D. Huxley, and J. P. Attfield, Chem. Commun. **003**, 3634 (2008).
[33] G. F. Chen, T. L. Xia, H. X. Yang, J. Q. Li, P. Zheng, J. L. Luo, and N. L. Wang, Supercond. Sci. Technol. **22**, (2009).
[34] H. Ogino, Y. Matsumura, Y. Katsura, K. Ushiyama, S. Horii, K. Kishio, and J. Shimoyama, Supercond. Sci. Technol. **22**, 075008 (2009).
[35] X. Zhu, F. Han, G. Mu, P. Cheng, B. Shen, B. Zeng, and H.-H. Wen, Phys. Rev. B **79**, 220512 (2009).
[36] N. Katayama, K. Kudo, S. Onari, T. Mizukami, K. Sugawara, Y. Sugiyama, Y. Kitahama, K. Iba, K. Fujimura, N. Nishimoto, M. Nohara, and H. Sawa, J. Phys. Soc. Japan **82**, 123702 (2013).

[37] H. Yakita, H. Ogino, T. Okada, A. Yamamoto, K. Kishio, T. Tohei, Y. Ikuhara, Y. Gotoh, H. Fujihisa, K. Kataoka, H. Eisaki, and J. Shimoyama, J. Am. Chem. Soc. **136**, 846 (2014).
[38] J. Yu, T. Liu, B.-J. Pan, B.-B. Ruan, X.-C. Wang, Q.-G. Mu, K. Zhao, G.-F. Chen, and Z.-A. Ren, Sci. Bull. **62**, 218 (2017).
[39] J. Paglione and R. L. Greene, Nat. Phys. **6**, 645 (2010).
[40] S. Fujitsu, S. Matsuishi, and H. Hosono, Int. Mater. Rev. **57**, 311 (2012).
[41] P. J. Hirschfeld, M. M. Korshunov, and I. I. Mazin, Reports Prog. Phys. **74**, 124508 (2011).
[42] J. W. Harter, H. Chu, S. Jiang, N. Ni, and D. Hsieh, Phys. Rev. B **93**, 1 (2016).
[43] T. Xie, D. Gong, W. Zhang, Y. Gu, Z. Huesges, D. Chen, Y. Liu, L. Hao, S. Meng, Z. Lu, S. Li, and H. Luo, Supercond. Sci. Technol. **30**, 95002 (2017).
[44] M. Brylak, M. H. Möller, and W. Jeitschko, J. Solid State Chem. **115**, 305 (1995).
[45] X. Wu, S. Qin, Y. Liang, C. Le, H. Fan, and J. Hu, Phys. Rev. B − Condens. Matter Mater. Phys. **91**, 1 (2015).
[46] Z. T. Liu, X. Z. Xing, M. Y. Li, W. Zhou, Y. Sun, C. C. Fan, H. F. Yang, J. S. Liu, Q. Yao, W. Li, Z. X. Shi, D. W. Shen, and Z. Wang, Appl. Phys. Lett. **109**, 1 (2016).
[47] T.-M. Chuang, M. P. Allan, J. Lee, Y. Xie, N. Ni, S. L. Bud'ko, G. S. Boebinger, P. C. Canfield, and J. C. Davis, Science **327**, 181 (2010).
[48] M. Y. Li, Z. T. Liu, W. Zhou, H. F. Yang, D. W. Shen, W. Li, J. Jiang, X. H. Niu, B. P. Xie, Y. Sun, C. C. Fan, Q. Yao, J. S. Liu, Z. X. Shi, and X. M. Xie, Phys. Rev. B − Condens. Matter Mater. Phys. **91**, 1 (2015).
[49] W.-C. Lee and C. Wu, Phys. Rev. B **80**, 104438 (2009).
[50] S. Raghu, A. Paramekanti, E. A. Kim, R. A. Borzi, S. A. Grigera, A. P. Mackenzie, and S. A. Kivelson, Phys. Rev. B **79**, 214402 (2009).
[51] M. Gao, F. Ma, Z.-Y. Lu, and T. Xiang, Phys. Rev. B **81**, 193409 (2010).
[52] Z. Wang, D. Walkup, Y. Maximenko, W. Zhou, T. Hogan, Z. Wang, S. D. Wilson, and V. Madhavan, Npj Quantum Mater. **4**, 43 (2019).
[53] K. McElroy, J. Lee, J. A. Slezak, D. H. Lee, H. Eisaki, S. Uchida, and J. C. Davis, *Atomic-Scale Sources and Mechanism of Nanoscale Electronic Disorder in Bi2Sr2CaCu2O8+δ* (2005).

[54] R. C. Dynes, V. Narayanamurti, and J. P. Garno, Phys. Rev. Lett. **41**, 1509 (1978).
[55] A. Sala, H. Yakita, H. Ogino, T. Okada, A. Yamamoto, K. Kishio, S. Ishida, A. Iyo, H. Eisaki, M. Fujioka, Y. Takano, M. Putti, and J. Shimoyama, Appl. Phys. Express **7**, 073102 (2014).
[56] Z. T. Liu, X. Z. Xing, M. Y. Li, W. Zhou, Y. Sun, C. C. Fan, H. F. Yang, J. S. Liu, Q. Yao, W. Li, Z. X. Shi, D. W. Shen, and Z. Wang, Appl. Phys. Lett. **109**, 130006 (2016).
[57] B. D. Josephson, Rev. Mod. Phys. **46**, 251 (1974).
[58] S. H. Joo, J.-J. Kim, J. H. Yoo, M. S. Park, K. S. Lee, G. Gu, and J. Lee, Nano Lett. **19**, 1112 (2019).
[59] M. H. Hamidian, S. D. Edkins, S. H. Joo, a. Kostin, H. Eisaki, S. Uchida, M. J. Lawler, E. -a. Kim, a. P. Mackenzie, K. Fujita, J. Lee, and J. C. S. Davis, Nature **532**, 343 (2015).
[60] A. Andreev, Sov. Phys. JETP. **20**, (1965).
[61] J. A. Sauls, Philos. Trans. R. Soc. A Math. Phys. Eng. Sci. **376**, 20180140 (2018).
[62] A. F. Otte, M. Ternes, K. von Bergmann, S. Loth, H. Brune, C. P. Lutz, C. F. Hirjibehedin, and A. J. Heinrich, Nat. Phys. **4**, 847 (2008).
[63] M. Ternes, A. J. Heinrich, and W.-D. Schneider, J. Phys. Condens. Matter **21**, 053001 (2009).
[64] V. Mourik, K. Zuo, S. M. Frolov, S. R. Plissard, E. P. A. M. Bakkers, and L. P. Kouwenhoven, Science (80-.). **336**, 1003 (2012).
[65] B. Jäck, Y. Xie, J. Li, S. Jeon, B. A. Bernevig, and A. Yazdani, Science (80-.). **364**, 1255 (2019).
[66] D. Wang, L. Kong, P. Fan, H. Chen, S. Zhu, W. Liu, L. Cao, Y. Sun, S. Du, J. Schneeloch, R. Zhong, G. Gu, L. Fu, H. Ding, and H.-J. Gao, Science (80-.). **362**, 333 (2018).

국 문 초 록

최초의 철 기반 초전도체가 2006년에 발견된 이후로 다른 타입의 철 기반 초전도체가 여럿 발견되었으며, 초전도 메커니즘을 이해하기 위해 그것들에 대한 많은 이론적 계산 및 실험이 진행되었다. $Ca_{0.9}La_{0.1}FeAs_2$는 2013년에 발견된 물질로 고유한 As 지그재그 층과 위상 초전도체의 가능성 때문에 실험적 이론적인 관심을 끌었다. 그럼에도 불구하고 아직 주사형 터널링 현미경 (STM)을 이용한 결과는 보고되지 않았다.

이 논문에선 $Ca_{0.9}La_{0.1}FeAs_2$ 시료에 대한 최초의 STM 결과를 보였다. 가능한 4개의 표면들이 모두 관측되었으며 각각은 지형 이미지, 전도율 맵, 전도율 스펙트럼을 이용하여 확인하고 각 표면의 고유한 성질들에 대해 연구하였다. FeAs 층에선 네마틱한 모습이 관측되었으며 그것들이 d_{xz}, d_{yz} 궤도 상태 성질을 갖고 있음을 보였다. As 지그재그 체인 층 위에 있는 칼슘 레이어는 비균질한 갭의 분포를 보였으며, 전도율 맵은 아래의 Ca 층에 있는 La 도펀트들을 보여주었다. 또한 상관관계 분석을 통해 La 도펀트가 국소적으로 초전도 현상을 약화시키는 것을 확인하였다. FeAs 층 위에 있는 Ca 층은 표면에 있는 틈을 통하여 표면 재구성이 일어나지 않은 FeAs 층을 직접 관측할 수 있는 가능성을 보여주었다. As 지그재그 체인 층에서는 푸리에 변환을 이용하여 Dirac 콘 분산을 보였는데 그것은 이 층의 고유한 성질이다. 제로바이어스 전도율 봉우리가 FeAs 층 위에 있는 Ca 층의 틈 위에 있는 As 지그재그 체인 층 에서 관측이 되었다. 위상 절연체에 초전도 근접 효과가 위상절연체에 적용 된 가능성 외에 다른 아는 가능성들은 제거 되었다. 제로 바이어스 전도율 봉우리는 이 시료에서 어떠한 실험을 더 해야하는지 방향을 제시한다.

주요어: 철 기반 초전도체, 주사형 터널링 현미경, 네마틱 성질, 제로 바이어스 전도율 봉우리.
학번: 2013-20362

감사의 말

심사를 해주신 김창영 교수님, 김기훈 교수님, 양범정 교수님, 심지훈 교수님 그리고 지도교수인 이진호 교수님 에게 감사의 말씀을 드린다.

같이 STM1에서 실험을 한 이경석, 주상현 두 동료에게도 정말 고마운 점이 많다. STM1이 설치 되기 전부터 같이 밤 새면서, 주말에도 나와서 납땜하고, 릭 테스트를 하였으며 설치 된 후에도 많은 시간을 함께 고생하며 STM의 정말 많은 부분들을 함께 한 소중한 동료들이다. 또한 이 연구실의 주요 공사를 맡은 박민석 형에게도 감사의 말씀을 전하고 싶다. 기초 공사가 잘 되었기에 좋은 결과를 얻을 수 있었고 그것을 기반으로 졸업을 할 수 있었다. 지금은 고생하는 중이지만 이 상황이 곧 끝나고 좋은 날이 올 것을 의심하지 않는다. STM이 제대로 돌아가기 전에 오셔서 정말로 큰 도움을 주신 박수현 박사님께도 정말 감사하다. 아무것도 모르는 아이들에게 많은 것을 가르쳐 주어 STM을 문제없이 운용을 할 수 있게 되었다. 일찍 석사졸업하고 떠난 곽정수에게도 많은 도움을 받았다. 만들어둔 간 많은 프로그램들은 수정하여 상당히 유용하게 사용을 했다. I would like to thank Dr. Haibiao Zhou. Although it was just a year, I learned a lot from his attitude and diligence as a professional. 그리고 연구실에서 인연이 닿은 전세계, 박성준, 송정근, 윤영훈, 유정훈 에게도 감사의 말을 남긴다.

매주 같이 식사를 하며 즐거운 시간을 보냈던 07학번 동기들에게도 정말 고맙다. 길진 않은 시간이었지만 정말 즐거웠고, 그 시간을 통해 다양한 사건들을 다양한 시각으로 바라 볼 수 있는 기회도 가질 수 있었다.

올 3월부터 시작한 논문쓰기모임 멤버들에게도 감사하다. 습관의 개선을 통해 효율적인 논문 작성을 할 수 있게 되었다.

마지막으로 오랜 시간 응원해준 가족들에게 감사의 말을 전한다. 덕분에 무사히 박사 졸업을 할 수 있게 되었다.